Dragonfly Preparation for Powered Flight Wind Tunnel and CFD Modelling

Peter Lorber
LM Fellow

Brian Wallace
Aeronautical Engr, Staff

Kalki Sharma
Aeronautical Engr, Sr

Patrick Bowles
Computational Aero, Mgr

Sikorsky, A Lockheed Martin Company, Stratford, CT

Karl Edquist
Senior Aerospace Engr
NASA Langley Research Center, Hampton, VA

Brian McGrath **William Kellermeyer**
Senior Professional Staff
Johns Hopkins Applied Research Laboratory
Laurel, MD

Paul Gilles
Test Engineer
National Full Scale Aerodynamics Complex, Moffett Field, CA

ABSTRACT

Preparation for Powered Flight (PPF) is a critical phase for Dragonfly, the National Aeronautics and Space Administration (NASA) mission to Saturn's moon Titan. During PPF the descending lander has been lowered below the backshell and uses its rotors to remove or "despin" any residual yaw motion of the vehicle. A 1/2-scale model of the Dragonfly PPF configuration was tested in the National Full-Scale Aerodynamics Complex (NFAC) 80 by 120-foot wind tunnel to measure aerodynamic loads and surface pressures on the lander and backshell. The results were used to improve understanding of the complex aerodynamic interactions and provide validation data for the Computational Fluid Dynamics (CFD) simulations used to develop the required aerodynamic databases for full-scale, Titan conditions. Configurations tested in the wind tunnel included Lander-alone-no-rotors (L), Lander-alone-with-rotors (LR), and Lander-with-rotors-and-Backshell (LRB). Both LR and LRB configurations were tested at multiple descent velocities and pitch and roll attitudes. The eight powered rotors were operated in nine combinations of active and inactive rotors, using steps of increasing RPM from idle to maximum. The results were used to identify conditions that generated the desired yaw moment for despin, and those that generated reduced or opposite sign moment. In parallel, CFD simulations applied the STAR-CCM+ toolset to the experimental geometry. Time-averaged virtual disks added spatially varying axial and rotational momentum to the flow to represent the rotors. There was generally good agreement between experiment and CFD, but conditions having strong interactions between the rotors, Lander, and Backshell were found to require more sophisticated methods. These lessons are being applied to the CFD for the full-scale Lander under Titan conditions.

INTRODUCTION

Dragonfly is a NASA New Frontiers mission led by the Johns Hopkins University Applied Physics Laboratory (APL) to study prebiotic chemistry on the surface of Titan, Saturn's largest moon, using a relocatable rotorcraft lander, as discussed in Ref. (1) and (2). Getting the lander to the surface requires a precise Entry, Descent, and Landing (EDL) sequence starting with separating the cruise stage, atmospheric entry, deployment of parachutes, and heat shield jettison, as shown in Figure 1. The lander is then posed (lowered) below the backshell to allow the rotors to spin, beginning the Preparation for Powered Flight (PPF) phase. During PPF pairs of rotors will be used to reduce residual spin of the vehicle prior to releasing the lander and initiating the Transition to Powered Flight (TPF) phase. During TPF, the lander falls for one second, spins up its rotors, and transitions to level flight, Ref. (3), (4), (5). After TPF, the lander descends, searches for a safe landing site using Light Detection and Ranging (LiDAR) sensors and cameras, and lands for the first time. The PPF phase is the focus of the experimental and computational efforts described in this paper. NASA Ames and Langley have primary responsibility for developing the EDL phase, with implementation supported by APL, LM Space, and Sikorsky. Dragonfly is scheduled for launch in July 2028 and arrival at Titan in late 2034, followed by a roughly three-year science mission.

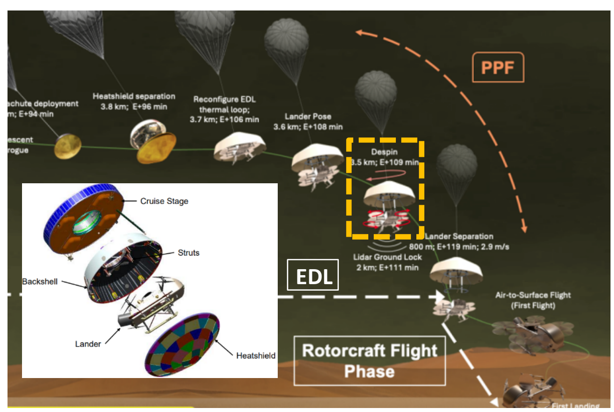

Figure 1. Dragonfly Entry, Descent and Landing phase.

The PPF sequence is a unique portion of EDL and includes requirements that reflect the need to understand the state of the posed lander during use of the rotors and prior to lander

Presented at the Vertical Flight Society's 81st Annual Forum & Technology Display, Virginia Beach, VA, USA, May 20-22, 2025.

release, to ensure high likelihood of a successful TPF sequence. One aspect of PPF that required special attention was the use of computational fluid dynamics (CFD) methods to predict the aerodynamics of the combined LRB configuration with and without spinning rotors, a continuation of efforts started in Ref. (6).

Given the unique nature of the PPF sequence and the fact that no relevant test or flight aerodynamics data from previous EDL missions existed for building confidence in the CFD methods for PPF, tailored wind tunnel testing was conducted by the Dragonfly EDL team to generate such data. Previous Dragonfly wind tunnel tests have used NASA Langley facilities to investigate entry vehicle aerodynamics, coaxial rotor pair aerodynamics and vibratory loads, and powered lander aerodynamics for TPF and forward flight conditions.

The 80- by 120-ft section of the National Full Scale Aerodynamics Complex (NFAC), operated by the United States Air Force (USAF) at NASA Ames Research Center, was chosen for Dragonfly PPF testing. The large test section was attractive because it to minimized wall interaction at low speed simulated descent. The test article included an approximately ½ scale model of the backshell and the lander with eight powered rotors. The parachute was not included. The test was conducted in December 2023 to February 2024 by a team from NASA, APL, NFAC, and Sikorsky.

Computational Fluid Dynamics (CFD) modelling of Dragonfly in the Titan environment is critical to designing the vehicle and its flight control systems. Validation with wind tunnel data increases confidence and reduces uncertainty in the CFD-based aerodynamic databases required for the PPF and rotorcraft flight phases. The primary CFD for database generation couples a steady Navier-Stokes flow field solution with blade element based virtual disk models of the rotors, as discussed in Ref. (7). More sophisticated unsteady and discrete blade models are also used as part of a multi-fidelity CFD workflow, see Ref. (8).

EXPERIMENTAL METHODOLOGY

The success of the test depended on integration of the NFAC wind tunnel, anemometry towers, and model positioning system with the separately developed models of the lander and its rotors and the backshell. Each hardware element had its own set of instrumentation with software for calibration, data acquisition, real time monitoring, and post-test analysis. The eight rotors had independent speed control. Effective application of the experimental results required quantitative estimates of the uncertainty and appreciation of the relevant scaling parameters.

Test Facility

The NFAC configured to use the 80- by 120-ft indraft test section is shown in Figure 2 from Ref. (9). Standard facility instrumentation includes a probe system to obtain an averaged static pressure and total pressure at the test section inlet, Ref. (9), plus measurements of barometric pressure, total temperature, and relative humidity. A weather station is installed at tunnel centerline height on a tower located 295ft upstream of the inlet plane. This weather station measures atmospheric wind speed and direction.

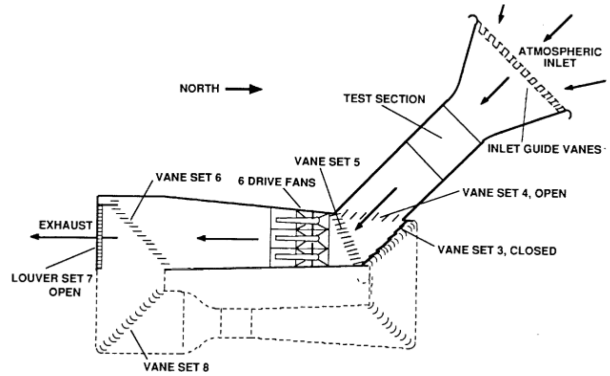

Figure 2. NFAC configured for 80-x 120-ft testing

These measurements are converted into centerline parameters by regular calibration, most recently in 2019. Figure 3 shows how the systematic uncertainty of q_∞ obtained using the static/total pressure system grows for q_∞<5psf and is unquantified below 1psf. This systematic uncertainty is dominated by measurement uncertainties in the transducers plus the uncertainty reported for the centerline pitot/static calibration probe.

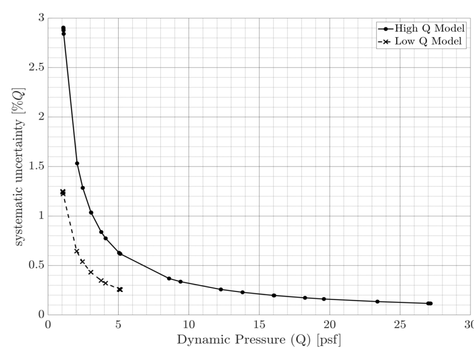

Figure 3. Systematic uncertainties for the 80- by 120-ft centerline dynamic pressure.

The desired free stream velocities were 4 to 6.9m/s (q_∞=10-30Pa or 0.2-0.6psf), in order to overlap Titan climb to hover induced velocity ratios, assuming maximum rotor RPM of 1100 for Titan and 3800 at NFAC. These were below the calibrated operating range of the standard system. To accurately measure and set such low velocities, two 20ft tall towers were installed 69ft upstream, 27ft from each wall. The installation is depicted in Figure 4. Each tower mounted four RM Young 81000 3-axis ultrasonic anemometers and two multi-instrument weather stations. A test-specific calibration was performed relative to a 3-axis Gill anemometer mounted at the model location. Calibration runs were performed at each nominal speed across a variety of ambient conditions, as well as for perturbed conditions.

A first-order combination of the two top 3-component anemometers mounted on each tower yielded the best performance across the calibration dataset (Table 7) and was implemented for the test. The 95% confidence uncertainty was ±0.3m/s. Test conditions could typically be set within

±0.15m/s. Testing was conducted in the late evening/night to maximize productivity in prevailing weather conditions. Testing was paused whenever the atmospheric wind speed and direction created unacceptable variation in the velocities.

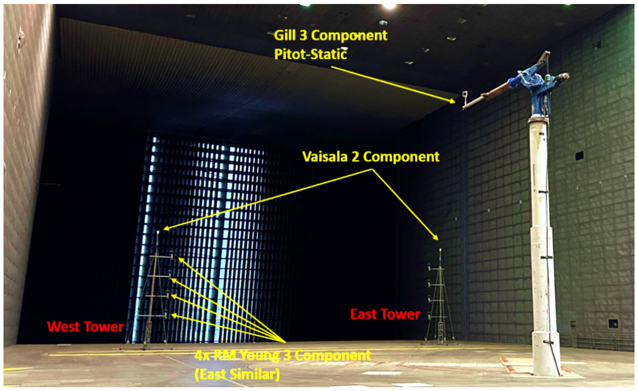

Figure 4. Low speed anemometer calibration

Table 1: Anemometer Calibration Model Results

Anemometers Used	*Cal Residual σ [kt]*	*Check Data σ [kt]*	*Check Data Bias [kt]*
Top 2 (Avg)	0.071	0.081	-0.011
Top 2 (Ind)	0.070	0.080	-0.012
Top 4	0.066	0.085	-0.029
Top 6	0.066	0.087	-0.026
All 8	0.053	0.083	-0.034

Dragonfly Model

The ½ scale Dragonfly lander model represented the 2023 configuration of the full-scale lander but was not strictly geometrically scaled. The geometry was based on the Integrated Test Program flying drone and this model was originally used for a prior test in the NASA Langley 14x22. The vertical fins and the cradle used to attach the pose mechanism were added. The pose mechanism itself was not included. The Lander model has a nominal length of 1.95m and was designed and fabricated by APL. The similarly scaled Backshell model has a diameter of D=2.6m and was fabricated by NASA Langley. The Lander and Backshell each have dedicated 6-component force and moment balances. The interface hardware includes two independent stings to capture each non-metric balance taper. The Lander sting passes through the Backshell model with clearance to avoid fouling the two metric systems.

Figure 5 shows the Lander plus Backshell (LRB) configuration from upstream at the left, and a top view of the Lander (LR) at the right. Figure 6 shows the model positioned at test section mid-height, mounted to an NFAC variable pitch mechanism which in turn was mounted to the test section yaw mechanism The mid-point of the model was above the yaw table axis of rotation, 15ft (4.5m) ahead of the vertical strut.

Figure 7 shows a definition of the pitch and roll motions, the lander coordinate axis, and the numbering system and rotation directions for the rotors. The test envelope was +50° to +130° lander pitch and -5° to +30° lander roll. At 90° pitch and 0° roll the bottom of the lander pointed upstream (toward the tunnel inlet), simulating a pure axial descent.

Figure 5. LRB and LR models installed

Figure 6. Installation overview, looking downstream

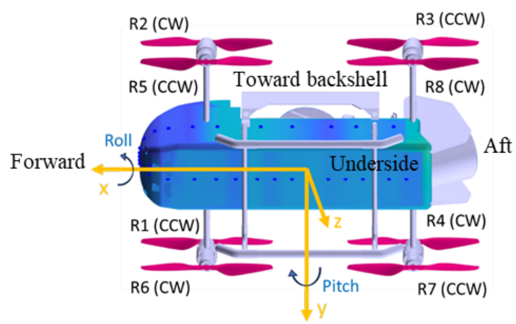

Figure 7. Lander axis and rotor definitions

The model had eight 30.5in. diameter, two-bladed, constant pitch, variable RPM rotors. The carbon fiber blades were purchased from KDE Direct, who also provided the blade geometry information for CFD validation. Each rotor was attached directly to a 5.7kW, three-phase, brushless outrunner drive motor. Each rotor pair was coaxial, counter-rotating, and canted laterally 5° bottom-out. The four rotors on the left side of the lander were mounted on ATI Industrial Delta 6-component load cells. Figure 9 shows the arrangement for one counter rotating rotor pair.

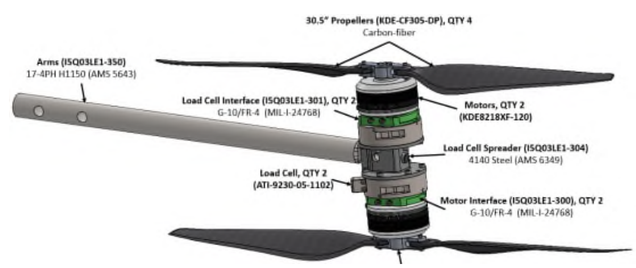

Figure 8. Coaxial rotor pair assembly

Model Rotor Control and Data Acquisition

Precise and stable rotor speed control was essential for the collection of quality data. The test matrix required rotor control from 0 to 3800RPM at shaft torques from zero to 4.9Nm. Model rotor speed control was established by incorporating eight independent Elmo model G-DRU100/100 Electronic Speed Controllers (ESCs) located remote to the model to alleviate volumetric constraints. Renishaw incremental encoders were incorporated within the motor sub-assemblies to provide relative rotor/motor position measurements. The ESCs minimized speed error with a tuned speed control loop utilizing differentiated position measurement as velocity feedback. The speed loop was carefully tuned to minimize overshoot or oscillations that could excite model dynamic responses that would contaminate balance and load cell measurements.

The large distance (90-ft) between the ESCs and the motors presented two challenges for routing the motor lead wires. First, the driving voltage supplied to the ESCs was set sufficiently high to overcome resistive and inductive losses in the cables. Second, routing 24 current carrying conductors (3 phases x 8 motors) from the ESC to the motors presented the risk of bridging the metric model frame to the non-metric sting that held the model. Ideally all model loads are designed to pass from the model frame through the balance to the sting. In reality, all sensor and motor conductors must also pass from the metric model frame to the sting. Care was taken to minimize this bridging through the careful positioning of a service loop. Check load pull tests were conducted to confirm minimal bridging after final assembly.

Speed commands were sent to the eight ESCs from a remotely located host computer that was operated by a model pilot through a custom software interface developed in LabVIEW. The software operated in either manual or automatic mode. In manual mode, the model pilot would pre-populate individual motor speed commands as prescribed by the test director/test matrix and simultaneously send the commands to the eight rotors. In automatic mode, the model pilot selected and initiated a preprogrammed rotor RPM sequence.

Each rotor RPM sequence was comprised of independent time series speed commands for each rotor. Table 2 lists the primary sequences utilized in testing. The "Active Rotors" step through a series of RPM commands and hold for enough time to assure stable speed control before proceeding to the next step and RPM. The remaining rotors hold at idle speed (380 RPM) for the entirety of the RPM sequence. The specific RPM steps were prescribed by the test matrix to satisfy test objectives. The automated rotor RPM sequences produce a multitude of unique model states in quick succession to minimize testing time.

This paper is focused on the Q1 and Q7 rotor sequences which despin the vehicle during PPF. Figure 9 provides a graphic of the rotor state and desired system control moment.

Table 2. Rotor RPM sequences

Sequence	*Active Rotors*
ZF	All at 0 RPM
Q1, Q7	2 Diagonal Lower Rotors R5+7, R6+8
Q5	4 Diagonal Rotors
Q6	4 CCW Rotors
A5	8 Rotors

RPM= 380 (idle) to 3800 (max)

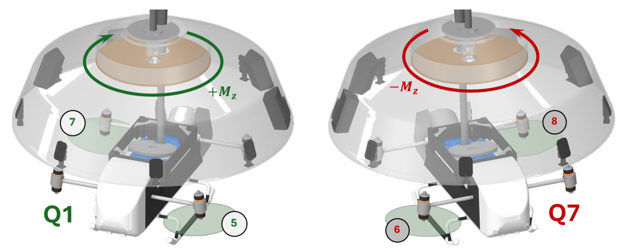

Figure 9. Q1 and Q7 operating rotors and intended system torque for PPF despin. Q1 produces a +M_z and Q7 produces a -M_z.

The model control software was designed to minimize model pilot fatigue for sustained testing. Figure 10 shows the organized layout of the model control and real time data interface. This single interface controls both rotor speed commanding and data recording.

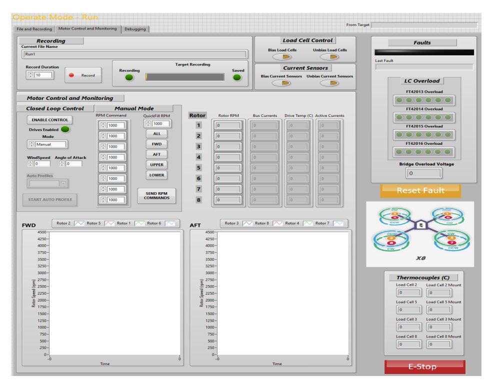

Figure 10. Model software control interface

Both the ATI load cells and the NASA balance were sensitive to large amplitude model dynamic oscillations that could exceed their load limits. In consideration of these instruments, the model control software included multiple safety features. These features include an automated rotor stop for the cases of rotor velocity limit exceedance, load cell limit exceedance, and NASA balance limit exceedance. For safety considerations, the model pilot also had the options of triggering either a software stop sequence or pressing an emergency stop button that disconnected power to the ESCs.

APL's Data Acquisition System (DAS) recorded motor ESC telemetry which included motor speed, bus voltage, ESC bus current, and ESC temperature. The APL DAS also recorded ATI load cell force, moment and temperature data. Thermocouples were placed on either side of each ATI load cell to measure the temperature gradient through the load cell.

The temperature gradient was monitored by the model pilot and testing was paused when the gradient exceeded 4°F as recommended by the load cell manufacturer to assure accurate load cell data.

In summary, this experiment employed a sophisticated rotor control system to manage the eight powered rotors of the 1/2-scale Dragonfly model. The system utilized three-phase brushless outrunner drive motors, ESCs, and a custom software interface to achieve precise control over rotor speed and sequence execution. By carefully designing and implementing the rotor control and data acquisition systems, the experiment was able to collect high-quality data on the aerodynamic interactions between the rotors, lander, and backshell, which is essential for understanding the complex dynamics involved in the PPF phase.

Lander and Backshell Instrumentation

The Lander and Backshell force and moment balances were provided by NASA Langley Research Center and were specified as model LRC-716-1K-1.50A and LRC-711B, respectively. They are single-piece direct-read 6-component balances which were calibrated at Langley in 2023. Table 3 shows the full scale (FS) load ranges and calibration accuracy.

Table 3. Model balances range and accuracy

Lander	*NF (N)*	*AF(N)*	*PM(Nm)*	*RM(Nm)*	*YM(Nm)*	*SF(N)*
FS Range	4448	890	288	113	113	2224
Accuracy (%FS)	0.08	0.20	0.06	0.24	0.14	0.09
Backshell	NF(N)	AF(N)	PM(Nm)	RM(Nm)	YM(Nm)	SF(N)
FS Range	2224	2224	435	81	239	1557
Accuracy (%FS)	0.49	0.39	0.11	0.42	0.11	0.14
Rotor	Fx(N)	Fy(N)	Fz(N)	Tx(N)	Ty(N)	Tz(N)
FS Range	660	660	1980	60	60	60
Accuracy (%FS)	1.25	1.25	1.50	1.00	1.25	1.75

The force and moment loads in the balance-axis systems were converted to model body- and wind-axis systems. This process includes translation, rotation, and converting all moments to right hand rule. Figure 11 shows the three primary body axis systems for F_x, F_y, F_z, M_x, M_y, and M_z, aligned in direction but translated in z.. The individual rotor forces and moments were reported initially in shaft axes, rotated to remove the cant, and then translated to the lander body axes.

In addition to the force and moment measurements, there were 55 Lander static pressure taps and 49 Backshell taps, shown by the markers in Figure 12. These were acquired using two 64-port electronic pressure scanners, one for the Lander and one for the Backshell. The calibration accuracy was ±0.06% of the 2500Pa (0.36psi) full scale. The reference was the tunnel barometric manifold, as measured by an absolute pressure sensor installed at the sting head.

Care was required because the aerodynamic pressures were normally of the order q_∞ = 10-30Pa, small compared to the hydrostatic pressure, $\rho g h \sim 150$ Pa, between the sting and the barometer in the control room and the ~10^5 Pa range of the absolute pressure transducers. Reference readings for all scanner ports and the two absolute sensors were taken at an initial wind-off, rotors-off condition and subtracted from the wind-on measurements.

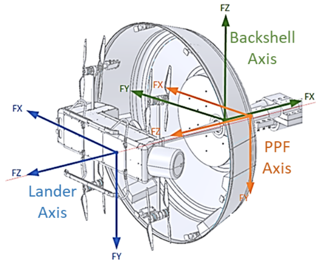

Figure 11. Lander and backshell body axes.

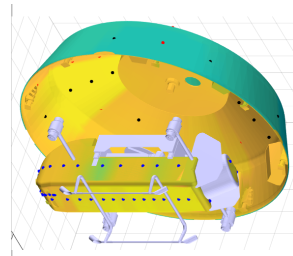
Figure 12. Pressure tap distributions.

The reported pressures are the differential relative to freestream static, P-P_∞, and the pressure coefficient C_P = (P - P_∞) / q_∞. The pressures were scanned at a rate of 10Hz, giving a potential unsteady bandwidth of up to 5Hz. The frequency response from the 25-100 cm pneumatic lines was estimated using the method of Ref. (10), which converts the unsteady Navier-Stokes equations to a one-dimensional wave equation having an analytical solution. The first resonance is at 65 to 350 Hz and for 10 Hz and below the amplification ratio is less than 1.03, indicating that the unsteady pressures could be used for at least qualitative purposes.

The relatively sparse tap distribution was interpolated onto surface patch representations of the Lander and Backshell and colored by the time averaged pressure, as in Figure 12. This proved to be quite useful for developing understanding of the load measurements and correlating to CFD. The grey surfaces had no pressure taps.

Wind Tunnel Data Acquisition

The NFAC Data Acquisition System (DAS) was used to acquire the outputs from both internal balances, the standard and supplemental wind tunnel instrumentation, and model attitude surface pressures. Critically, a synthetic nominal rotor RPM signal was acquired from the APL DAS to synchronize the two datasets. In addition to acquiring the raw signals, the NFAC DAS was programmed to reduce the measurements to critical parameters. The data reduction included standard balance computations, coordinate transformations, weight tares, and tunnel condition computations (using the test-specific calibration). The NFAC DAS was configured to acquire analog signals, including the balance raw outputs, at 2KHz. Data from digital instruments, including the model surface pressure measurements, were recorded at 10Hz.

The primary test objective was to produce a set of body force and moment measurements across a variety of pre-scripted rotor control sweeps and attitudes. The volume of test conditions posed practical challenges for researchers due to the primary data (body force & moment, rotor performance) being split between the APL DAS and the NFAC Steady DAS and Basic DAS. The first challenge was synchronizing the acquisition start and the duration between the systems to ensure all desired data were collected. This challenge was solved with a straightforward "take data" trigger and by administratively adjusting the NFAC DAS point duration to encompass the rotor sequence being executed. The second challenge was to identify each RPM step and align the three data streams. As shown in Figure 13, the rising edge of the RPM signal in each stream was used to align the start times. Manual review was required to resolve noise spikes on the NFAC RPM signal, inconsistent skew in clock times, truncated point durations, and missing, mis-placed, or corrupted data files. Data alignment, application of data corrections, and generation of statistical and time series files was performed post-test by Sikorsky.

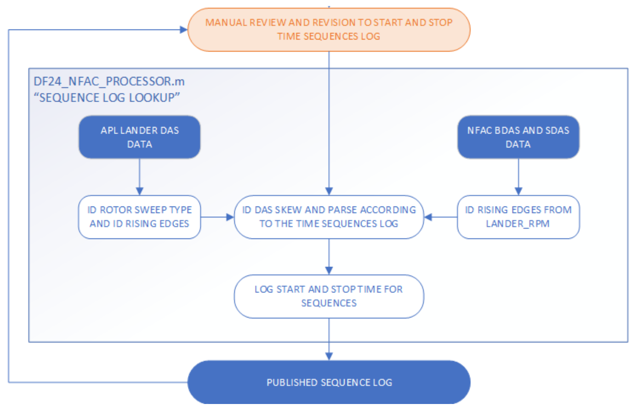

Figure 13. Merger of NFAC and APL data acquisition streams

Test Conditions

Testing was completed across 26 runs spanning just over 1 month. One major model change (adding the Backshell) took approximately a week midway through testing. The approach to data collection was to set freestream velocity and model pitch and roll, and then step the RPM up and back down for each selected rotor operating sequence (Table 2).

Figure 14 shows the pitch/roll (P/R) test points for four primary rotor sequences: Zero Hold (ZH) with all rotors at 0 RPM, Q1 and Q7 with diagonal lower rotors spinning and stepped in RPM with the other 6 rotors at idle, and A5 with all eight rotors stepped at the same RPM. A total of 13,051 specific combinations of velocity, pitch, roll, rotor sequence, RPM, and model configuration were acquired.

Experimental Uncertainty

Data processing procedures for this test were devised to minimize errors and uncertainties, but due to the nature of wind tunnel testing, inaccuracies are assured. The uncertainty can be divided into two components: systematic uncertainty (U_r) and precision uncertainty (U_s). Systematic uncertainties are largely derived from calibration of the wind tunnel conditions and lander, backshell, and rotor balances.

Precision uncertainty (data reduction uncertainty) lends itself to varied interpretation. Figure 15 gives an example of the process used in this paper to determine precision uncertainty. A sequence in the dataset was extracted to produce a waveform duration which was representative of that test condition, typically 4-8s. The waveform is processed through a 0.5s running average to produce an assessment on the variation of the average during that period. The precision uncertainty error bars shown in plots in this paper correspond to the 95% (2σ) confidence interval from the running average.

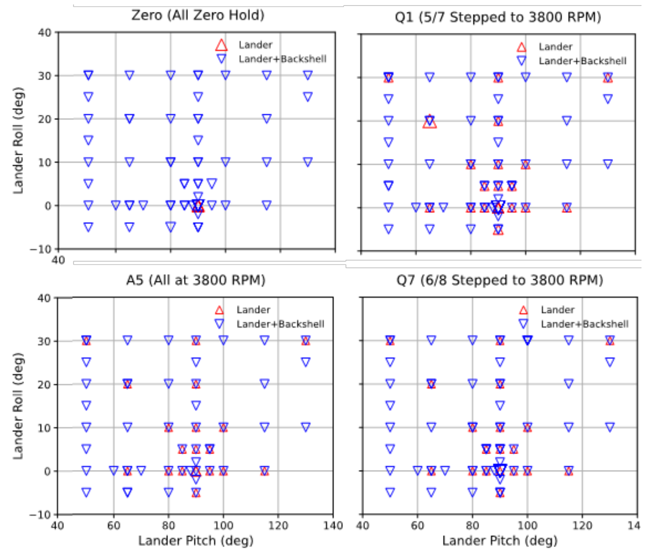

Figure 14. Test condition matrices for ZH, Q1, Q7, and A5 sequences at V_∞ = 5.3m/s

The resultant of systematic uncertainty and precision uncertainty is the total uncertainty reported in this paper.

$$U \approx \sqrt{{U_s}^2 + {U_r}^2}\,.$$

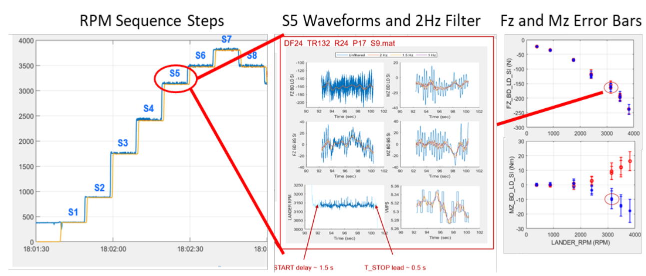

Figure 15. Sequence analysis and uncertainty example

Gas Properties, Scaling and VRS

The most relevant scaling parameters for this test are Reynolds number, Mach number, and the ratios between the freestream and the rotor tip and induced velocities. Table 4 compares gas properties at NFAC in air, at Titan, and at the NASA Langley Transonic Dynamics Tunnel (TDT) in R-134A heavy gas. The TDT is included since it was used for prior full-scale Dragonfly rotor tests, Ref (11).

Freestream velocities were set so that Titan and NFAC freestream dynamic pressures and Mach numbers were reasonably close, q_∞ ~10-30Pa and M_∞ ~0.01-0.02, as shown in Table 5. Compared to Titan, the combined scaling of density (0.22), velocity (1.8), geometry (0.5) and viscosity (2.7) leads to a 10-15x difference in Reynolds number, $\rho V_\infty D/\mu$. Since Re is still greater than 800,000 and the geometry is angular, separation locations should be generally consistent, with the possible exception of the outside of the backshell at high pitch or roll angles. Viscous shear forces are no more than 5-10% of the pressure forces, based on selected CFD solutions.

Table 4. Titan and wind tunnel conditions

	P_∞ $10^5 Pa$	T K	ρ kg/m^3	μ, 10^{-5} $kg/(m\text{-}s)$	a m/s
NFAC	1.01	293	1.2	1.81	339
Titan, 4 km	1.19	89	4.6	0.64	203
Titan, surface	1.47	94	5.4	0.67	195
TDT	1.01	303	4.0	1.24	170

Table 5. NFAC and Titan scaling using freestream velocity and Backshell diameter, D

V_∞ m/s	q_∞ Pa	Mach U_∞/a	Reynolds (V_∞, D)
4.0	10	0.010	8.0 x10^5
5.3	17	0.016	1.1 x10^6
6.9	29	0.020	1.4 x10^6
3.0 Titan	24	0.015	1.3 x10^7

Rotor RPM was set so blade tip Mach numbers were similar to those at Titan, M_{tip}~ 0.4. Ratios were maintained between V_∞, $V_t=\Omega R$, and hover induced velocity, v_h=Thrust/$\sqrt{2\rho\pi R^2}$. Table 5 compares model scale rotor properties at NFAC with those at 1100RPM at Titan. The 10-15x reduction in chord Reynolds number is the same. Also shown for reference are nominal values for single rotor thrust and v_h.

Table 6. NFAC and Titan scaling using rotor tip speed and chord at 75% radius

RPM	V_t m/s	Mach V_t /a	Re (V_t $c_{.75}$)	T_{1R} N	v_h m/s
1200	49	0.14	1.7 x10^5	12	3.0
2400	97	0.29	3.3 x10^5	50	6.5
3800	154	0.45	5.2 x10^5	120	10.0
1100 Titan	78	0.40	5.6 x10^6	400	5.1

Since PPF is a descent condition with rotors operating at varying RPM, penetration into Vortex Ring State (VRS) is an important consideration. VRS has been extensively studied, e.g., Refs (12), (13), but data for coaxial rotors next to a wall (the Lander) and below a solid shell is limited at best. Figure 16 shows how the ratio of climb velocity, V_C= -V_∞, to hover induced velocity, v_h, aligns to the Ref. (13) single rotor model as the flow state varies from hover (V_C=0m/s) through mild to severe (red) VRS. The vertical axis is the ratio of actual power to hover power. All tested conditions measured the rotors absorbing power, rather than operating in a windmill brake state.

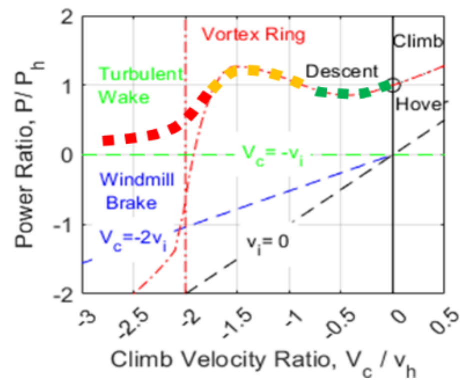

Figure 16. Rotor flow states adapted from (12) and (13)

COMPUTATIONAL METHODOLOGY

The CFD aerodynamic database is used in the flight dynamics simulations of the lander in the APL developed Closed Loop Simulation (CLS) and NASA Program to Optimize Simulated Trajectories II (POST2) tools. Over 3000 simulations are required to populate the database. That number of simulations necessitates a multi-fidelity CFD workflow that strikes a balance between computational efficiency and accuracy. Currently, mid-fidelity CFD is used for the database while high-fidelity is used for cross-checks. The NFAC test vs. CFD validation quantifies the error as uncertainty of the PPF aerodynamics. That uncertainty is then scaled to Titan conditions and used with the Titan CFD database in CLS and POST2. The use of mid-fidelity CFD is, of course, a risk – higher fidelity CFD is often more accurate in capturing complex physics. The multi-tool and multi-fidelity analysis is shown in Figure 17. CFD fidelity, accuracy, and resource expense increase left to right.

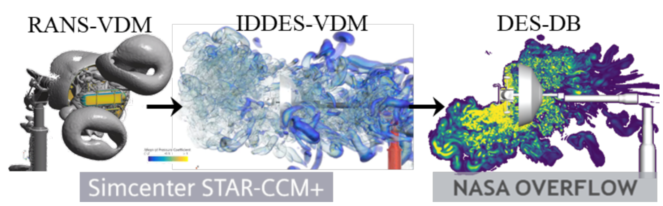

Figure 17. CFD methods used for the NFAC CFD validation, illustrated by vorticity visualizations.

STAR-CCM+ is a commercial, multi-physics software package. The mid-fidelity model used a coupled, implicit steady-state Reynolds Averaged Navier Stokes (RANS) solver. The volume discretization used a second order, central differencing scheme with boundedness. The turbulence model was Spalart-Almaras (SA). The Virtual Disk Model (VDM) used for the rotors is described below. The combined methodology is denoted RANS-VDM.

Unsteady simulations in this paper maintain second order spatial discretization and use a second order dual-time stepping scheme with either unsteady RANS (URANS) or the SA Improved Delayed Detached Eddy Simulation (IDDES) turbulence model. When IDDES is used with the VDM, these results are denoted IDDES-VDM.

Due to the low Mach numbers of this test, constant density was used for both RANS and IDDES. All other solver settings, including the VDM and mesh described later, were constructed to follow the full-scale Titan CFD workflow described in Ref. (7).

High-fidelity CFD using NASA OVERFLOW (2.4) was also used to compare, contrast, and help understand the NFAC test results. Details and results are provided in Ref. (8). This approach used Detached Eddy Simulation and discrete blades, referenced as DES-DB in Figure 17.

To accomplish the large number of RANS-VDM simulations required to cover the attitudes and RPMs investigated in the test, a streamlined workflow was established to convert test conditions to CFD inputs, run the simulations, and collect the results. This workflow was also used in Ref. (7). Batches of 50 cases were distributed across multiple High Performance Computers (HPC) and scheduled using Design Manager within STAR-CCM+. Individual simulations were set up to stop once the windowed average of the yaw moments of the rotors, lander, and backshell were each within a specified asymptotic tolerance. The simulations were set to run from a minimum of 1750 up to a maximum of 8000 iterations.

Domain and Components

The CFD model included the Dragonfly lander and backshell, support structures, and the wind tunnel domain. An image of the components is shown in Figure 18. The tunnel domain consisted of a rectangular prism to model the 80 x 120ft NFAC wind tunnel. CFD boundary conditions are shown in Figure 19. Because of the small size of the model (0.1% blockage), and avoiding operation with high inlet cross flows, the inlet contraction was not modeled and the walls used inviscid slip boundary conditions.

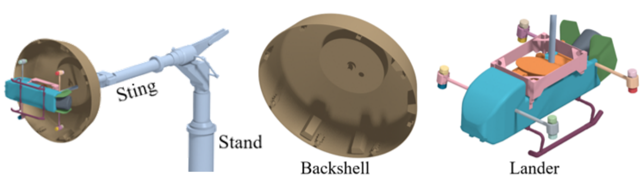

Figure 18. Dragonfly CFD model components and assembly.

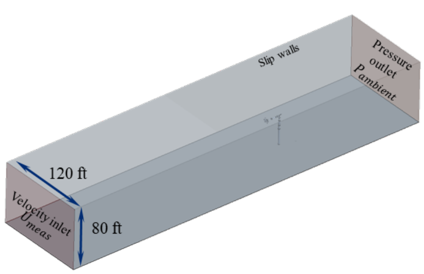

Figure 19. Computational domain used to simulate the Dragonfly NFAC installation.

The simulation ambient conditions (pressure and temperature), lander pitch and roll, rotor RPMs, and test section velocity were extracted from the experimental data and used for each simulation condition. This allows direct comparison to the measured forces to calculate error.

Rotor Model

The VDM simulates the aerodynamic effects of a rotor by representing it as a disk within the fluid flow. It utilizes Blade Element Momentum Theory (BEMT) to calculate time-averaged but spatially varying forces and moments on the disk elements from inputs such as rotation rate and rotor geometry. Blade section lift and drag forces are computed from local flow velocities and C81 airfoil coefficient tables generated using the OVERFLOW solver at test-appropriate Mach and Reynolds numbers, as in Ref. (14). The VDM settings and mesh are consistent with Ref (7). A half-cosine tip loss function was applied to the VDM model starting at r/R=0.85. Comparisons of STAR-CCM+ RANS-VDM to full-scale Dragonfly rotor forces and moments had correlation similar to that shown in Refs. (11) and (15) for RotCFD.

Mesh

An unstructured polyhedral mesher generated the surface and volume mesh. The surface mesh of the backshell and lander is shown in Figure 20. The cell size was chosen such that a minimum of five cells existed between two sharp edges, and all the intricate features of the internal components would be captured to avoid defeaturing. The near-body cross-section of the volume mesh is also shown in Figure 20. The boundary layer mesh settings were chosen to ensure a $y+$ of 1 at 5.3 m/s. The off-body volume mesh is shown in Figure 21. The tunnel walls had a cell size of 1 m, and refinement regions for the rotors' near- and far-wake and backshell had cells sizes of 0.022m, 0.044m, 0.022m, respectively. All the refinement regions rotate with the lander orientation except for the backshell wake region, which remains parallel to the tunnel axis to resolve its wake.

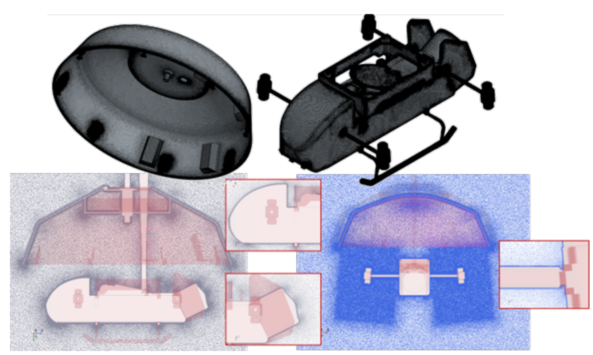

Figure 20. Surface meshes (top) and volume mesh slices at y=0 (bottom left) and through the forward rotors (right).

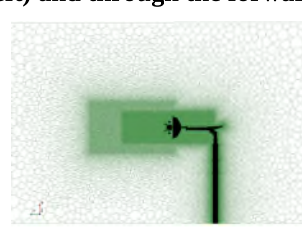

Figure 21. Volume mesh slice at y=0m.

Unmodeled Geometry

The CFD model does not include the following items:

- Lander motor and load cell wires
- Lander and Backshell openings or "leakages"
- Wires secured to the mounting stings
- Small fasteners, gaps, and other hardware features
- Blade attachment or hub
- Blade elasticity of the KDE blades

These omissions should have minimal impact on the overall aerodynamics, but potentially affect sensitive quantities, e.g. drag, in areas or conditions where flow separation is altered causing cascading impacts. Scans of the NFAC installation were not available, but images of the test and CFD geometry are compared in Figure 22. Several KDE blades were 3D scanned, showing modest blade-to-blade and blade-to-design differences such as flatwise bending deflections and hand sanding effects on the leading- and trailing edges. Overall the RANS-VDM thrust and torque will be shown to compare well to the rotor test data despite such nuances.

Figure 22. Test and CFD geometry comparisons

Discrete Blade Analysis

Analysis was also performed for a smaller subset of cases using discrete blades (DB) and the unsteady RANS (URANS) solver. Cases used a temporal resolution of 1° per timestep, 16 sub-iterations, and total time of 20 rotor revolutions. Averages were taken over the last 4 revolutions. Two rotors are set up for simulation (R3 and R8). Figure 23 contains images of the rotors, off-body mesh, and the surface mesh.

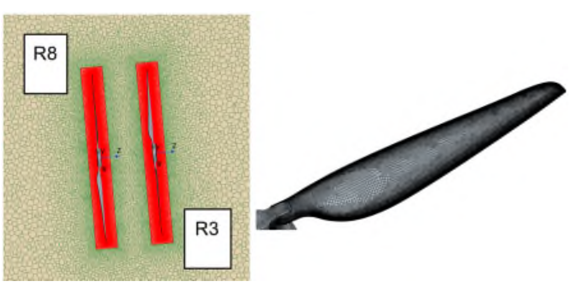

Figure 23 Surface and volume mesh for isolated rotor discrete blade (DB) setup.

EXPERIMENTAL RESULTS

Lander-Only (L)

The first configuration tested was the lander without the backshell or rotor blades (L). Figure 24 shows the body axis forces (as defined in Figure 7) as a function of the roll and pitch attitude, all at V_∞=5.3m/s. Variations are small for ±10° from axial descent, P/R = 90/0°. At higher angles, F_x and F_y forces from wind axis drag appear. The lower image shows pressure coefficient values and mapped colors at P/R=90/0°. Yellow is stagnation on the lower surface, C_P=1.

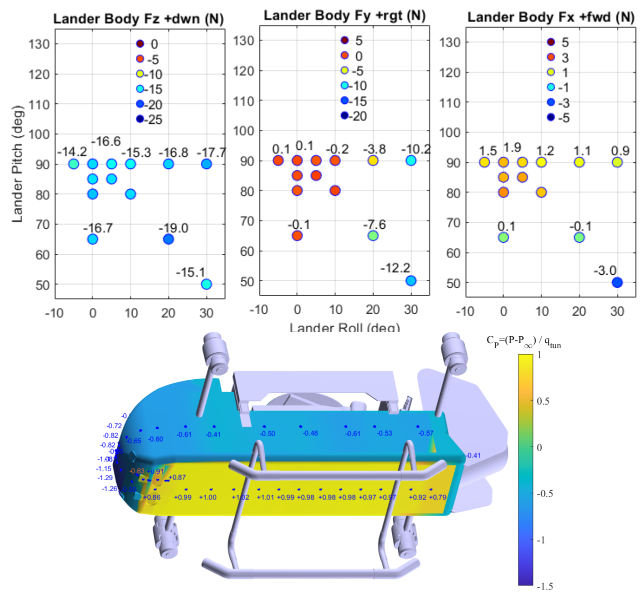

Figure 24. Lander without rotors (L) body-axis forces vs. Pitch and Roll at V=5.3m/s and C_P at P/R=90/0°

Lander Plus Rotors (LR)

Figure 25 shows the F_z (thrust/drag) force and M_z (yaw) moment as functions of rotor RPM in axial descent, P/R=90/0°. The upper row shows the sum of lander and rotor loads in body axis. The blue and black symbols are for sequences Q1 (Rotors 5 and 7 active) and Q7 (Rotors 6 and 8 active) in hover at V_∞=0m/s. The loads increase quadratically from idle at 380 RPM to a maximum of F_z= -240N at 3800 RPM with M_z= +16Nm for Q1 and -16Nm for Q7. As V_∞ is increased to 6.9m/s, the LR drag at idle increases to F_z=-55N. The variation in F_z with V_∞ is reduced at higher RPM as the rotor-induced velocities interact with the lander body.

The yaw moment varies with V_∞ and RPM depending on VRS penetration and rotor-lander interactions. For Q1 at V_∞=6.9m/s (red circles), M_z increases from 380 to 1000RPM, drops until 2000 RPM, and then rises to 15Nm at 3800RPM, compared to 16 Nm in hover. The VRS metric V_C/v_h is -1.9 at 1000RPM, -1.3 at 2000RPM, and -0.7 at 3800RPM. Consistent generation of M_z requires sufficient rotor thrust to achieve V_C/v_h > -1.2 and avoid strong VRS (Figure 16). At lower V_∞ this boundary is reached at lower RPM.

The lower row in Figure 25 shows Rotor 8 shaft axis F_z (thrust) and Mz (torque). The influence of V_∞ is small, implying only limited effects of VRS on the time averaged rotor loads themselves. The figure also shows the lander body axis M_z from Rotor 8, adding the moment from the 5° canted thrust to the shaft torque. The canted thrust contribution is ~2x that from shaft torque. Doubling the Rotor 8 M_z (-8Nm at 3450RPM and V_∞=5m/s) to account for the unmeasured Rotor 6 gives -16Nm from the rotors, compared to -11Nm for the entire vehicle, indicating that the lander body produces a +5Nm or -30% counteracting moment.

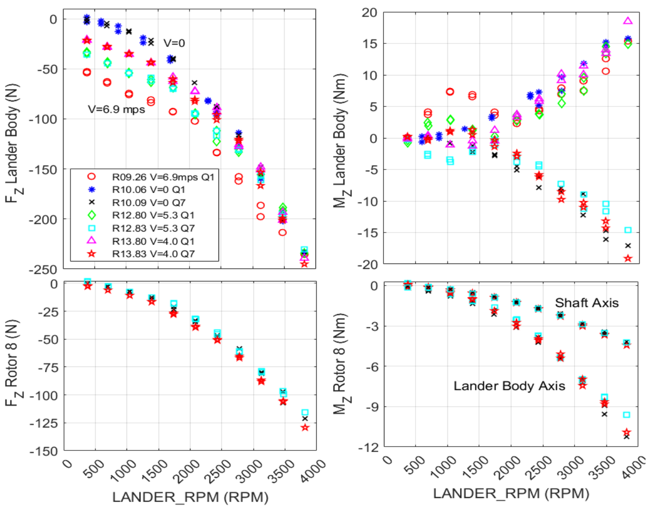

Figure 25. LR and Rotor 8 F_z and M_z for Q1 and Q7 at P/R=90/0°, V_∞=0, 4, 5.3, 6.9 m/s.

Figure 26 shows Lander surface pressures during the Q1 RPM sweep at V_∞=5.3m/s and P/R=90/0°. In the upper left, at 600 RPM and low thrust, the lower surface sees yellow stagnation pressures, and the sides and nose see moderate suction, C_P ~ -0.5. At 1400RPM, the increased rotor thrust generates much more forward suction. Integrating the yaw moment from the measured C_P produces an adverse M_z of 10Nm. As RPM increases further, the increased induced velocities from the rotors flip the pressures on the lower surface from stagnation to suction. This reduction in body drag is responsible for the lowered effect of V_∞ on F_z that was observed in Figure 25.

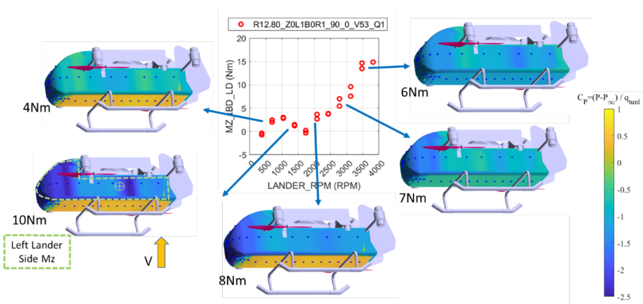

Figure 26. LR body C_P suction opposing rotor +M_z for sequence Q1 at V_∞=5.3 m/s and P/R=90/0°.

The effect of pitch and roll attitude on the lander plus rotors forces and yaw moment at 3450RPM, V_∞=5.3m/s is shown in Figure 27. Body axis F_z increases noticeably for P/R > ±10°. F_y and F_x are most affected by the respective roll and pitch angles, as expected. M_z maintains authority within ±20% for pitch within ±10° of 90° and roll below 25°, but M_z shows up to a 50% reduction at more extreme attitudes.

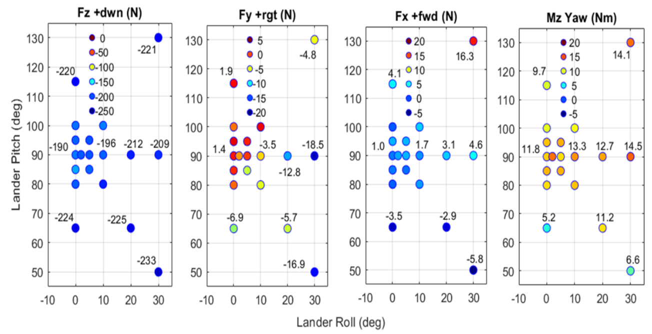

Figure 27. LR F_x, F_y, F_z, and M_z vs. pitch and roll for Q1 at 3450 RPM and V_∞=5.3m/s.

Lander Plus Rotors Plus Backshell (LRB)

After examining the LR results, the number of pitch/roll attitudes for the LRB test phase was increased to better define the despin envelope. The number of RPM steps was reduced, but the record at each step was increased to 8 seconds. Figure 28 shows F_z (top) and M_z (bottom) vs RPM for sequences Q1 and Q7 at V_∞=4.0, 5.3, 6.9m/s, P/R=90/0°. The LRB total is on the left, the LR in the middle, and the Backshell on the right. The LRB F_z shows a strong increase with V_∞ at RPM< 2500, which weakens at higher RPM, especially at lower velocities. The LR F_z trends are more consistent, reaching -250N at 3800RPM, similar to the Figure 25 results for the lander alone. The Backshell F_z (drag) weakens as rotor thrust increases, approaching zero at the lower velocities. This will be discussed further below.

The LRB and LR M_z in Figure 28 are low below 2000RPM, with consistent increases from 2500 to 3800RPM. At the highest velocity, M_z is reduced by up to 5Nm (25%). The backshell M_z is small, providing up to a 2Nm addition at 1750RPM, and up to a 1Nm reduction above 3000RPM.

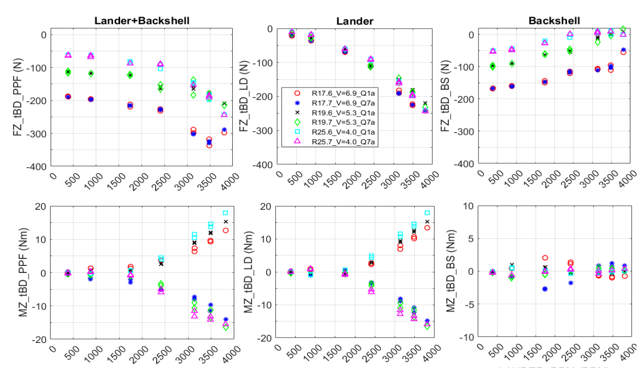

Figure 28. LRB F_z and M_z for Q1 and Q7 at P/R=90/0° and V_∞=4.0, 5.3, 6.9m/s.

Figure 29 shows the progression in surface pressures with increased RPM with and without the backshell. At idle, both the lander and the inside of the backshell are near stagnation pressure (C_P > +0.8), consistent with the measured near-zero lander F_z and strong negative backshell F_z (drag). As rotor thrust increases, the induced flow along the backshell into the rotors flips the pressure inside the backshell to a level of suction, $C_P \sim -0.5$, similar to outside the backshell, consistent with near zero backshell F_z. Compared to the LR pressures, with the backshell present the Lander lower surface stagnation pressure flips to suction at lower RPM, and the suction on the side does not get as strong or generate as strong an adverse M_z. This is consistent with the reduced adverse M_z seen in Figure 28 for the LRB.

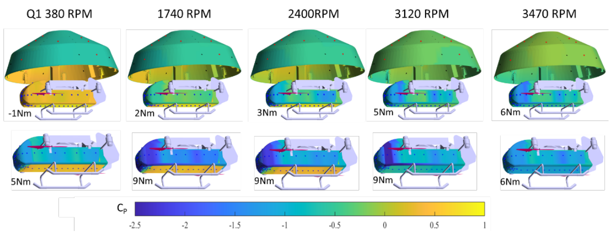

Figure 29. Comparison of LRB and LR pressures for Q1 at 380 to 3470 RPM, P/R=90/0°, V_∞= 5.3 m/s.

Shaft axis thrust and torque for Rotors 3 and 8 during Q7 sequences are shown in Figure 30. Runs 12 and 13 are LR and Runs 17-25 are LRB. There is very little difference for Rotor 8 (active), while F_z on Rotor 3 (idle) is slightly larger at V_∞=5.3 m/s without the backshell.

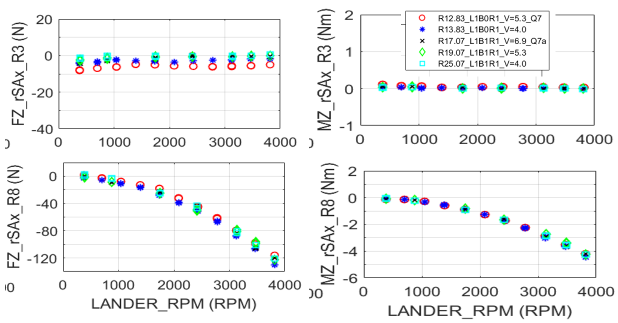

Figure 30. Rotor F_z and M_z with and without the backshell for Q7 at V_∞=4.0, 5.3, 6.9m/s, P/R=90/0°.

Varying the model pitch attitude can have a substantial effect on the loads, as shown in Figure 31 for pitch sweeps at zero roll. There is higher drag, $-F_z$, and reduced M_z at higher pitch and roll angles. M_z remains strongly positive from 65 to 130° pitch, but was significantly reduced at 50° pitch. The pressures show very strong suction at the nose, caused by a combination of freestream and rotor induced velocities. At zero RPM and 50° pitch, the nose suction is absent. The pressures also show that at the higher pitch angles of 50°,70°, and 115°, there is positive pressure on the inside of the backshell creating a drag force which combines with rotor thrust to generate F_z= -320N compared to -180N at low pitch.

The effect on F_z, M_z, and C_P of varying roll attitude from -5° to +30° is illustrated in Figure 32 for Q1 and Q7 sequences at 3480 RPM. For Q1, positive roll does increase nose suction up to C_P = -3.5. This is consistent with the measured 25% reduction in M_z. Q7 has a similar reduction in M_z, but the suction is not seen, likely because the aft fin and cradle are not pressure-instrumented. As with pitch, the higher roll angles allow the freestream to produce positive pressure on the inside of the backshell, increasing drag.

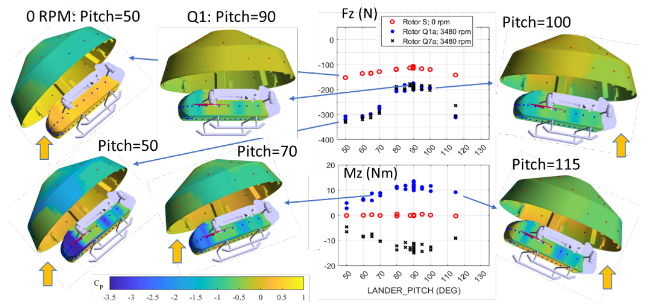

Figure 31. Pitch dependence of LRB F_z, M_z, and C_P for Q1 at 3480RPM, Roll=0, and V_∞= 5.3 m/s.

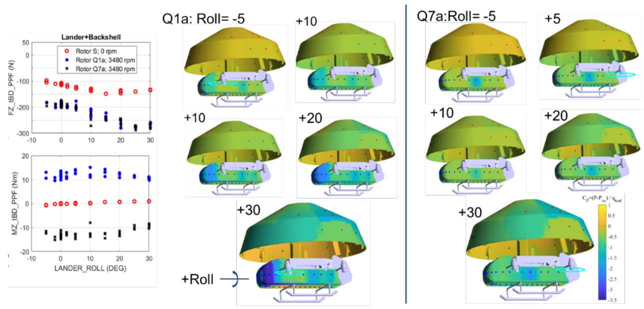

Figure 32. Roll dependence of LRB F_z, M_z, and C_P for Q1 at 3480RPM, Pitch=0, and V_∞= 5.3 m/s.

LRB forces and yaw moment for all measured attitudes are plotted in Figure 33, for Q1 at 3480 RPM and V_∞=5.3m/s. As noted above, F_z increases at higher pitch and roll, as the backshell drag is recovered. F_y and F_x are generally small at lower angles, and higher at higher angles. M_z authority is generally maintained for pitch attitudes of 80° to 130°, but substantially reduced at 60° and 50°.

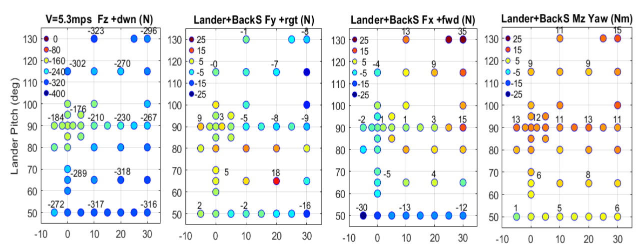

Figure 33. LRB F_x, F_y, F_z & M_z vs. pitch and roll for Q1 at 3480 RPM and V_∞ =5.3m/s.

Figure 34 compares M_z for Q1 at 3480 RPM for V_∞ = 4.0, 5.3, and 6.9 m/s. At the lowest speed there is a strong favorable yaw moment generated at all tested attitudes. At the highest speed, the region of strong favorable M_z is reduced to 90±15° pitch, and there is a region of adverse yaw moment at 50° pitch. As noted in the figure, the VRS metric, V_C/v_h increases from -0.4 at V_∞= 4m/s to -0.7 at V_∞=6.9 m/s. While all of these are below the axial flow stability boundary in Figure 16, Refs (13) and (5) do show that the boundary moves to reduced V_C/v_h when in-plane velocity is present, as occurs at larger pitch and roll angles.

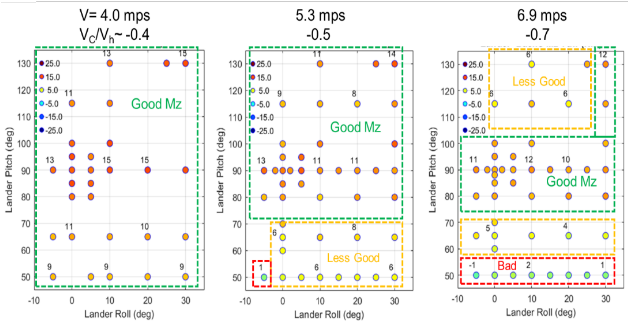

Figure 34. LRB M_z vs. pitch and roll for Q1 at 3480 RPM, and V_∞=4.0, 5.3, 6.9 m/s.

Unsteady Loads and Pressures

Figure 35 shows time histories of selected lander, backshell, and rotor loads, RPM, and V_∞ for a Q1 sequence at P/R= 90/0. Each step is ~8 seconds long, is shown in a different color, and had a 4Hz digital low pass filter applied. This format provides a qualitative indication of the unsteady content as rotor RPM varies. Lander unsteady amplitudes increased above 1750 RPM, and were generally higher during the reducing RPM half of the sequence. Backshell, F_z and F_x amplitudes were notably higher above 3000 RPM.

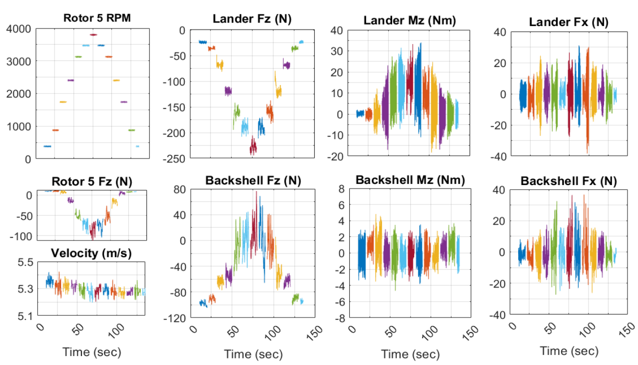

Figure 35. Lander, Backshell, and Rotor 5 load time histories for Q1 at P/R=90/0° and V_∞=5.3 m/s.

Figure 36 shows spectra for the three forces plus Mz at 3480RPM. The primary plots are not filtered and extend to 120Hz. The rotor 2p is present at 115Hz for the lander, plus model structural responses previously identified by rap testing of the installed model. The inset plots focus on the 0 to 4Hz range, consistent with the filtered time histories. The peaks near 0.5 to 1.0Hz observed for both Lander and Backshell forces are of interest since they are believed to represent unsteady aerodynamic interaction between the rotor-induced velocities, the Lander and Backshell wakes, and the external flow. The magnitudes at the 0-1Hz frequencies are ~3x higher for Backshell F_z than for Lander F_z.

A small number of test conditions were acquired for an extended record of 90 sec. Figure 37 shows lander and backshell F_z and surface pressure vs. time for a case with large rotor-backshell interaction: V∞=6.9 m/s, Q7 at 3480RPM and P/R=90/0°. The blue curves are unfiltered with 1kHz bandwidth, and the red curves have a 4 second moving block average applied. The backshell F_z has the highest amplitude low frequency variation, at 0.2 to 0.8Hz. This content is also seen at lower amplitude in the lander F_z and in the pressures on the inside of the backshell and the bottom of the lander. This again appears to be caused by interaction between the rotor wakes and the flow along the backshell. Further investigation using CFD will be described below.

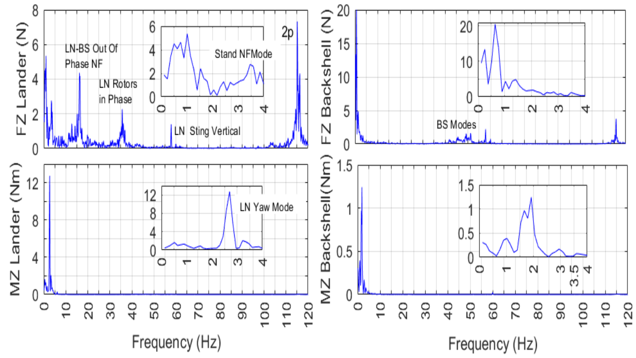

Figure 36. Lander and Backshell force and moment spectra for Q1 at 3480 RPM, V_∞=5.3 m/s, P/R=90/0°.

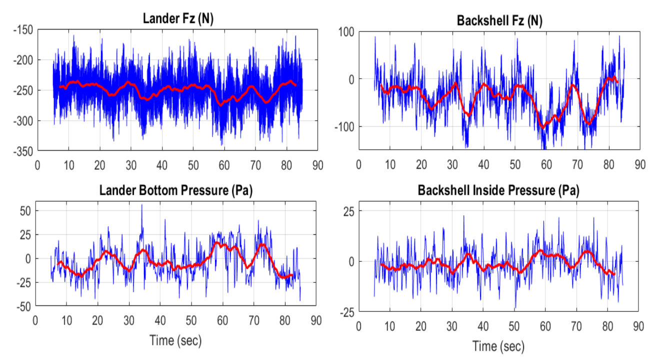

Figure 37. Extended record of Lander and Backshell F_z and pressure, for Q7 at 3840 RPM, P/R=90/0°, V_∞=6.9m/s.

COMPUTATIONAL RESULTS

In this section, the CFD results for the vehicle are compared with the wind tunnel data, with a focus on the metrics of vertical force, F_z, and yawing moment, M_z. The primary objective is to evaluate the correlation between the simulation results and wind tunnel measurements, while identifying methodologies to enhance the consistency and accuracy of the correlation.

Lander-only (L)

In Figure 38 the aerodynamic loads are plotted as a function of the roll and pitch attitude, all at V_∞=5.3m/s. The results are for the lander-only configuration (no backshell, no rotors). The RANS results show good trending with test, with F_x ~0.5N lower than the test and F_z ~1N lower. Additional mesh refinements (not shown) did not improve the correlation. Similar results were found at 4.0m/s and 6.9m/s.

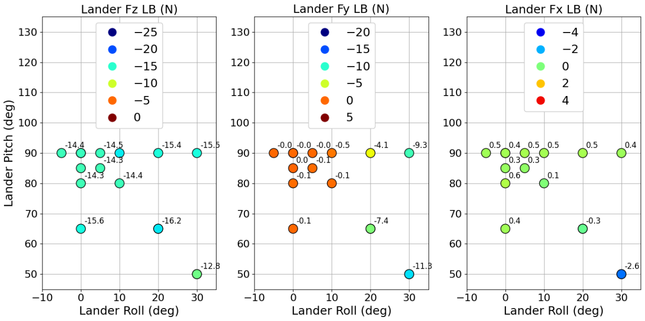

Figure 38. Lander-only loads vs. pitch at R=0, V∞=5.3m/s

Lander + Rotors (LR)

To present the LR correlation results, data is plotted across sweeps of rotor RPM, starting with the individual rotor thrust and torque results in Figure 39 to highlight the RANS-VDM ability to accurately model the rotor's installed physics. The shaded green region and the error bars correspond to the second standard deviation of the CFD iteration history and the second standard deviation of the test processed data as described previously. The shaded green region is not strictly physical for the RANS-VDM data, but instead indicate the solver's ability to converge to a single value in these difficult flow scenarios. The values above the F_z and M_z plots' x-axes are the difference between the test and CFD results. The largest error in rotor F_z is ~7.5%, and for M_z the RANS-VDM torque is within 0.2Nm. The in-plane rotor forces and lateral and longitudinal moments, though not plotted here, are relatively small, and well within the 1st standard deviation of the test error bars. Similar F_z and M_z correlations were observed across the test matrix.

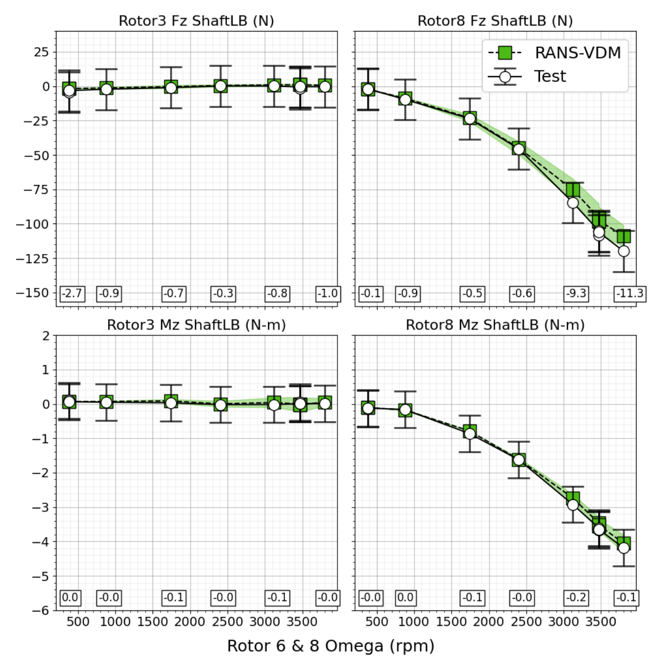

Figure 39 Rotor thrust and torque at P/R=90/0°, Q7, and V∞=6.9m/s

To further verify the VDM, isolated discrete blade cases were simulated for the A5 rotor sequence in descent at 6.9m/s. As outlined previously, only R3 and R8 were simulated. An isolated rotor was also set up for the RANS-VDM approach, and the computational results are compared with the rotor load cell, as shown in Figure 40. For the RANS-VDM and URANS-DB Rotors 3 and 8 torque predictions are within 0.2Nm for all cases. The computational torque also aligns well with test in trend and magnitude. Both computational methods under-predict Rotor 3 thrust for RPM<2500. At higher rotor speeds, both computational approaches capture the test data well, with the URANS-DB approach showing better agreement in Rotor 3 thrust, and RANS-VDM showing better agreement in Rotor 8 thrust. Overall, this effort provides confidence that in complex flow domains, such as VRS, the lower order VDM approach can provide adequate results for rotor thrust and torque.

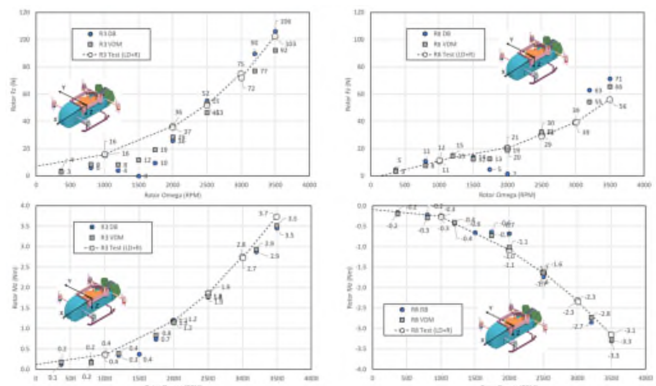

Figure 40. Comparison of RANS-VDM, URANS-DB, and test for R3 (left) and R8 (right) thrust and torque in descent at V∞=6.9m/s for the A5 rotor sequence.

The Q1 rotor rpm sequence during descent, P/R= 90/0°, and at a tunnel speed of 6.9m/s is illustrated in Figure 41. In these plots, the four of the six-component loads are plotted in the lander balance (LB) frame against the despin rotors' RPM (Rotors 5 and 7 in this case). The LR results at P/R=130/30° are plotted in Figure 42. The RANS-VDM results agree well with the test data F_z and M_z, even following some of the more subtle variations in the M_z as RPM increases. The error in F_z between the experimental and RANS-VDM data for both the P/R=90/0° and 130/30° datasets is approximately 4.7N, relative to peak loads of ~250N. For M_z, the error for the two orientations is ~1.2Nm, with peak yaw values of ~16Nm. The variance in the test data increases with rotor speed, indicating flow unsteadiness, as discussed in the experimental section at these conditions. As with the rotor balance correlation, the CFD and test in-plane loads are small, with CFD typically within 1-2σ.

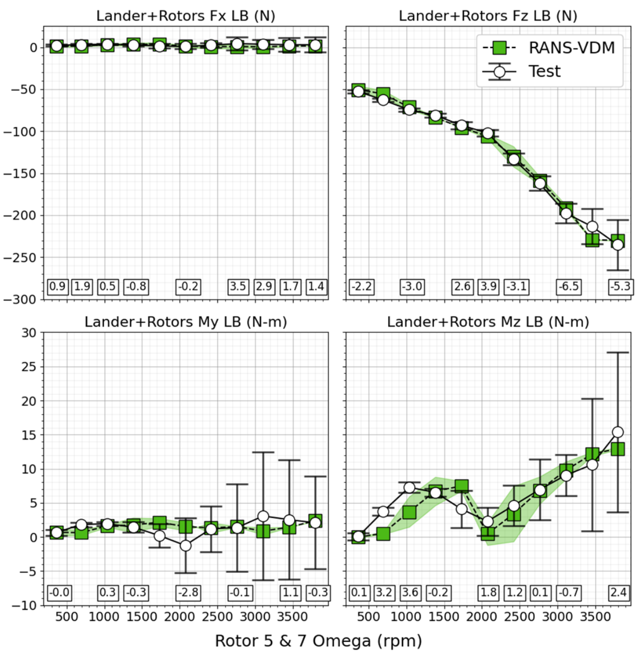

Figure 41. LR sequence Q1 at V∞=6.9 m/s, P/R=90/0°.

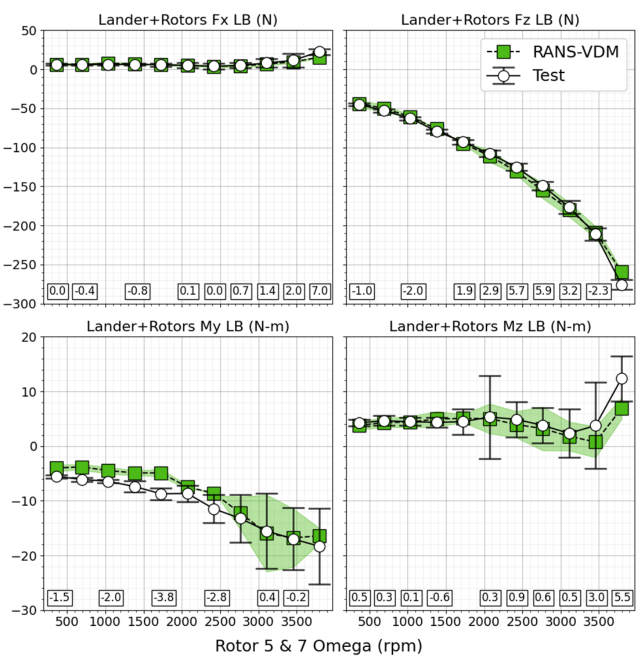

Figure 42. LR sequence Q1 at V∞=6.9 m/s, P/R=130/30°.

The impact of pitch and roll attitude on the LR forces and yaw moment at 3450RPM and V∞=5.3m/s is shown in Figure 43 where the color range is consistent with Figure 27. The first two columns present the RANS-VDM F_z and Test - CFD F_z, while the third and fourth show M_z. RANS-VDM underestimates F_z across all orientations by 10N to 40N, relative to peak loads of ~250N. The error is larger than that observed in the lander-only comparison, indicating growth related to the increasing complexity of the blade installation and rotor induced aerodynamic interactions. It accurately predicts the yaw moment direction of the vehicle with an average error margin of 1.7Nm, relative to peaks near 15Nm

In-plane forces show larger percent-error but are small in absolute magnitude compared to F_z. These loads are a stronger relative function of the non-modeled geometries in these conditions. For brevity, the in-plane loads are not plotted in the Figure 43 format; throughout the P/R angles investigated, in-plane forces and moment behave similar to that shown vs. RPM in, e.g., Figure 41 and Figure 42.

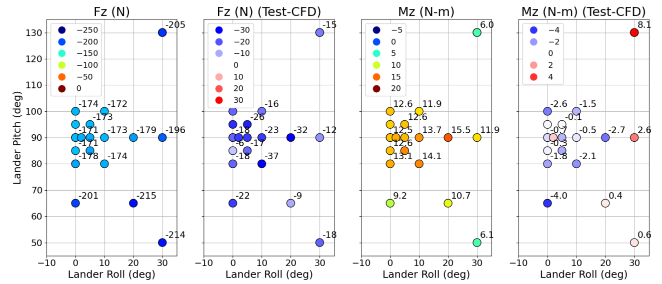

Figure 43. LR Q1 sequence at 3450RPM, V∞=5.3m/s, F_z and M_z vs. pitch and roll

The Test v. CFD error is shown for 2700RPM and V∞=5.3m/s in Figure 44. At this lower rotor speed, RANS-VDM still tends to underestimate F_z at an absolute error up to 12N relative to system loads of -150N. Overall, these correlations highlight the RANS-VDM ability to accurately capture the LR configuration F_z and M_z to within ~20% of the test data.

The RANS-VDM and test LR F_z and pressure contours for the P/R=80/10°, Q1, and V∞=5.3m/s conditions are shown in Figure 45. At 1740RPM, the RANS-VDM exhibits an F_z error of 2.5N compared to a test F_z of ~-65N. The error at 3400RPM in LR F_z is ~-20N relative to a test F_z of ~-240N. These errors are primarily due to differences in bottom plate pressure. At 3400RPM, RANS-VDM predicts $C_p \approx -1$, whereas the test measures $C_p \approx -0.3$. This disparity arises from rotor-lander interaction, which RANS-VDM can struggle to accurately model near descent orientation at higher rotor speeds. The F_z errors are similar at 3100 to 3800RPM.

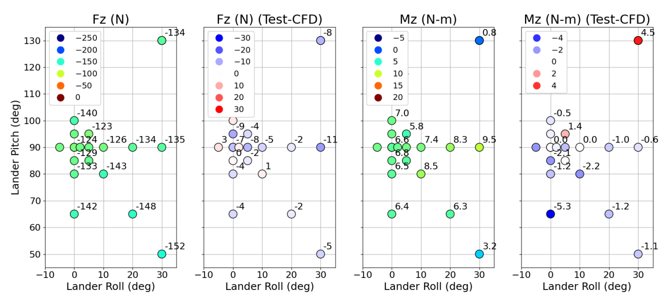

Figure 44 CFD Results for LR, Q1 at 2700RPM, V∞=5.3m/s, F_x, F_y, F_z, and M_z vs. pitch and roll

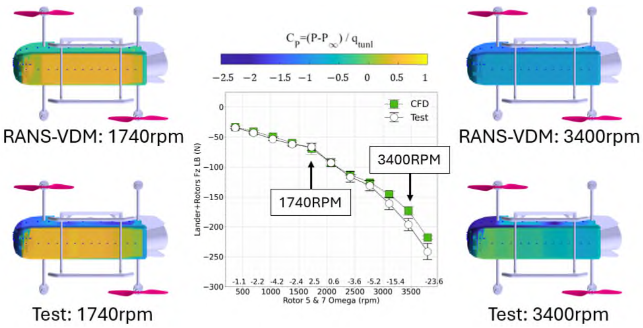

Figure 45. LR F_z and pressures: P/R=80/10°, Q1 sequence, V_∞= 5.3m/s.

Lander+Backshell (LRB)

Figure 46 plots the results for the PPF LRB configuration during descent at 6.9m/s, for a rotor speed sweep of the Q1 rotor sequence. The F_z (top row) and M_z results (bottom row) are displayed in the lander balance (LB) frame, with the first column showing the lander and the second column the backshell. There is a strong correlation between RANS-VDM and test data, except for the 3800RPM case where RANS-VDM overestimates F_z for the backshell by 87N. The 3800RPM condition also shows a growth in the test F_z σ bars caused by increased low frequency load fluctuations. RANS-VDM appears to lock onto a solution near the upper limit of the test oscillation range. This behavior will later be compared to the IDDES results.

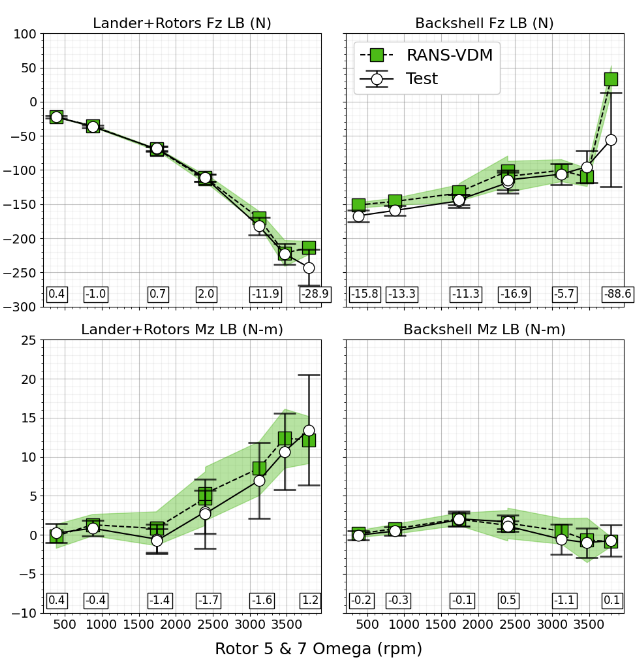

Figure 46. LRB F_z and M_z for rotor sequence Q1 at V_∞=6.9m/s, P/R=90/0°.

In the descent orientation, the rotors' wake acts in opposition to the wind tunnel flow entering the backshell while the rotors simultaneously reduce the pressure inside the backshell as they generate increasing thrust. At 3800RPM, both the test and RANS-VDM backshell F_z show a significant increase, driven by an internal backshell pressure change as depicted in in Figure 47. Both the test and simulation pressure contours show the pressure drop within the backshell, with the CFD results exhibiting a more pronounced change.

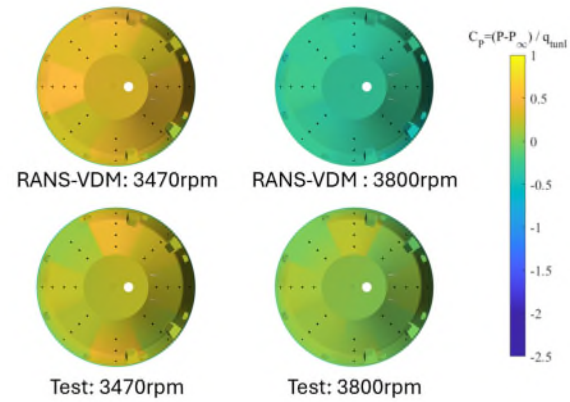

Figure 47. Backshell interior pressure at 6.9m/s, LRB descent orientation, sequence Q1 at 3470 & 3800RPM

Figure 48 plots results at 6.9 m/s, P/R=130/30°. In this orientation, the backshell does not exhibit the same increase in F_z at higher rotor speeds observed in straight descent. The rotors do not prevent the wind tunnel flow from entering the backshell, so that F_z is more influenced by tunnel speed than rotor speed. The RANS-VDM F_z error is minimal, as is the unsteadiness in the test data throughout the RPM sweep. The largest relative discrepancies are in lander M_z at RPM> 3000.

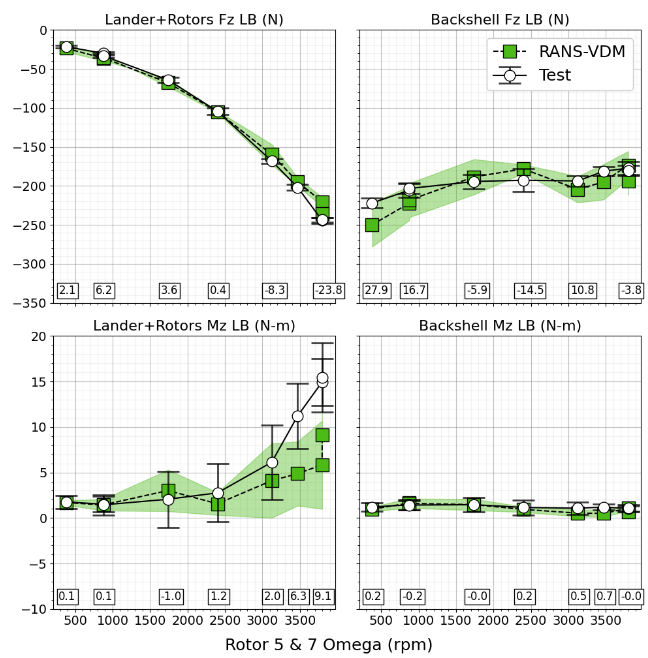

Figure 48. Lander (left) and Backshell (right) F_z and M_z for rotor sequence Q1 at V_∞=6.9m/s, P/R=130/30°.

Lander surface pressures are compared in Figure 49 for 2400 and 3800RPM. At 2400RPM, with RANS-VDM under-predicting lander M_z by 1.2Nm, the pressures are quite close to the test data. At 3800RPM, the RANS-VDM under-predicts lander M_z by 9.1Nm. The test provides pressure readings on the port side of the lander while there are RANS-VDM pressure contours on both sides. From these two views it can be seen that on the port side RANS-VDM under-predicts the pressure relative to the test, and on the starboard side it shows a negative pressure region on the tail. The lander shows a -M_z in both the test and RANS-VDM, but the stronger rotor induced negative pressure is likely the cause of larger -M_z lander contribution from RANS-VDM.

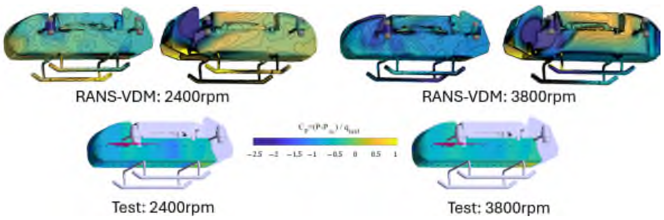

Figure 49. Lander pressures for Q1 at V∞=6.9m/s, P/R=130/30°.

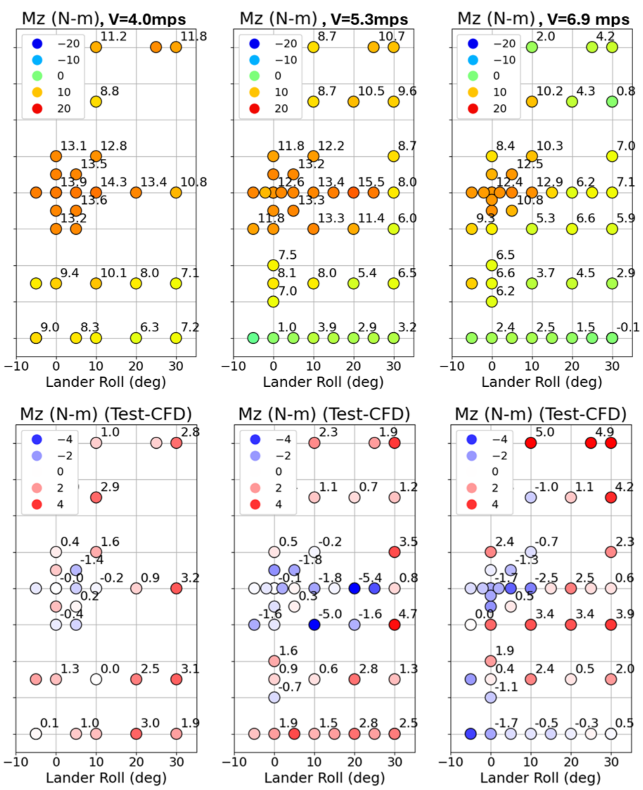

Figure 50. LRB M_z for Q1 at 3480RPM at V∞=4.0, 5.3, 6.9 m/s

The impact of pitch and roll attitude on the lander and backshell F_z and M_z at 3480RPM and V∞=5.3m/s is plotted in Figure 51. CFD under-predicts F_z relative to test with the greatest error near the P/R=90/0° descent orientation. The F_z error at higher P/R is significantly lower. The story is simpler for M_z: increased error is found at distinct incidences far from P/R=90/0°, at high descent velocity, and high RPM. This behavior is visualized by the 130° pitch data in Figure 50.

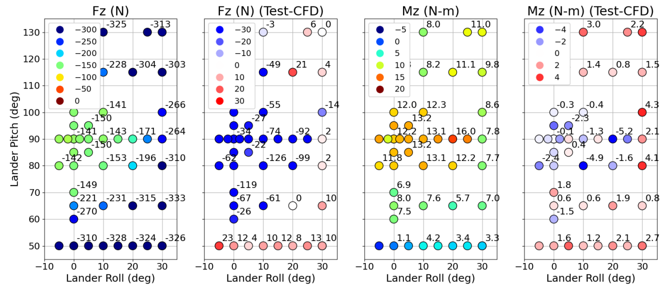

Figure 51. LRB F_z & M_z for Q1 at 3480RPM, V∞=5.3m/s

A lower rotor speed, 2400RPM, was also investigated to identify the effect of rotor thrust. Figure 52 shows the forces and yaw moment results. The error in F_z shows a significant drop in magnitude compared to 3800RPM, while the M_z errors at the orientation limits remains similar in magnitude.

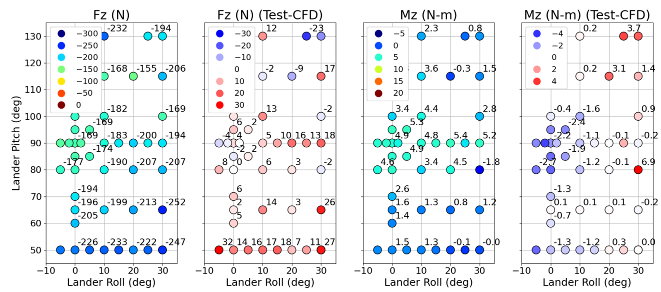

Figure 52. LRB F_z & M_z for Q1 at 2400 RPM, V∞=5.3m/s

Time-averaged F_z and M_z generally show strong correlation between RANS-VDM and test. Weaker F_z correlations arise at operating conditions with strong lander and rotor interactions with the backshell, typically at higher RPM when the vehicle is in descent at $V_C/v_h > -0.6$. These conditions can also have large Backshell oscillatory forces (Figure 37). Weaker M_z correlation occurs at higher pitch and roll orientations. The steady RANS-VDM trends parallel to the test data, but it struggles to adequately capture details of the flow physics and loses accuracy. This implies that higher fidelity unsteady methods such as IDDES-VDM are needed.

Unsteady Loads

To understand the impact of switching from RANS to IDDES, cases with both good and poor correlation were simulated using IDDES. The wake structure of the IDDES-VDM cases at P/R=90/0°, V∞=6.9m/s, Q1 rotor sequence, 3400RPM is shown in Figure 53. The flow demonstrates the complexity that IDDES is able to capture, which should better model the actual flow in the test run, as opposed to the RANS-VDM solver, which captures the average flow characteristics.

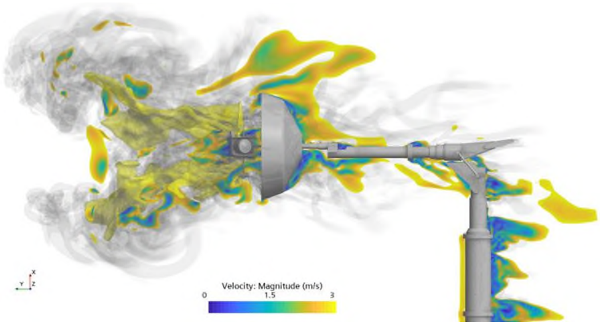

Figure 53 Wake structure for rotor sequence Q1, 3400RPM, V_∞=6.9m/s, P/R=90/0°.

Figure 54 shows Backshell F_z during descent at 5.3m/s for a rotor speed sweep of the Q1 rotor sequence. The figure plots Backshell F_z against rotor speed, with IDDES results as yellow stars plus violin plots of the IDDES solution history. At 1740RPM, the RANS-VDM and IDDES-VDM solutions converge to a similar value; each agrees with the test data. At 3400RPM, the RANS solution falls near the upper bounds of the IDDES solution while the mean of the IDDES agrees very well with the mean of the test data. As noted previously, the RANS results lock onto a state near the test maximum as well. The time-accurate IDDES solutions permit a more physical unsteady shed wake to form, which produces a time-averaged F_z much closer to experiment.

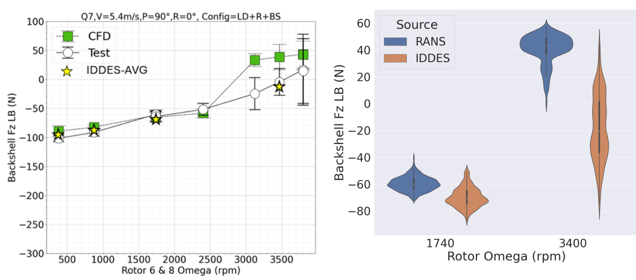

Figure 54. Backshell F_z for LRB Q7 Sequence at P/R=90/0° and V_∞= 5.3 m/s.

Figure 55 plots the lander M_z at P/R=130/30° and 6.9m/s for the Q1 rotor sequence. The error in M_z is highest for cases above 3000RPM. Rotor speeds of 2400RPM and 3800RPM were simulated using IDDES. The mean of the IDDES M_z shows substantial error reduction.

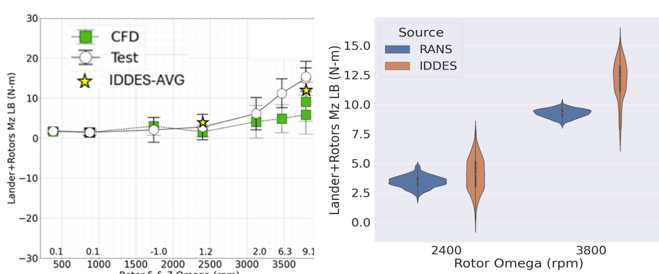

Figure 55. Lander M_z for P/R=130/30°, LRB Q1 at V_∞= 6.9 m/s.

DISCUSSION

The wind tunnel and accompanying CFD validation study provided valuable insights into the aerodynamics of the Dragonfly mission during the PPF phase. The NFAC test campaign verified that the yaw control authority required to null the spin rate of the Lander and Backshell prior to TPF was not always available. In combination with full-scale Titan CFD for both PPF and surface flight, this helped finalize the program decision to reorient the rotors to the configuration shown at the right of Figure 56, as described in Ref (7). The new configuration reduces adverse rotor-lander interactions and provides robust yaw authority throughout the expected mission envelope.

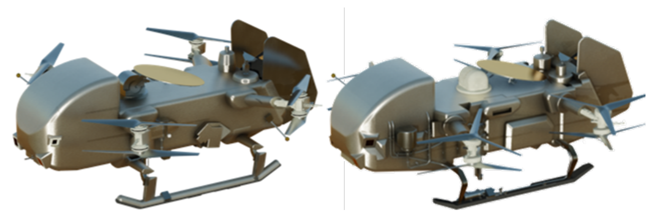

Figure 56. Renderings of 2023 NFAC model basis (left) and 2024 Critical Design Review configuration (right).

The many thousands of unique data points from the NFAC test provide a comprehensive database for CFD validation. The complex flow physics, which involve multi-body interactions, rotor-body interactions, body-rotor interactions, flow separation and bluff body shedding of numerous length scales represent a challenge to modern numerical methods which need to comprehensively and accurately model such phenomenon throughout the flight envelope. To focus on the scale of the validation performed here, parity plots of the RANS-VDM correlation for the primary F_z and M_z loads are shown in Figure 57. Here, test data and CFD are plotted directly against each other without attention to the underlying incidence, RPM, etc. CFD that correlates perfectly against test would show a line with unity slope and no variance. Clearly, the CFD is well correlated to the test data, although variance increases from the rotor loads to the LR, and then to the LRB, following the increasing complexity associated with the flow field and aerodynamic interactions with each step.

Although High Performance Computers are consistently growing, low- and mid-fidelity CFD methods are still required to team with high-fidelity methodologies once the number of CFD cases grow past a few dozen. The RANS-VDM method used here did well overall. Key errors were identified based on the test vs. CFD error and were studied with the IDDES-VDM approach. The introduction of IDDES improved the correlation against the test data while incurring a 5x increase in computational resources. A multi-fidelity approach, combining the RANS-VDM and IDDES-VDM is a cost-effective and accurate approach for the CFD required for Titan. High-fidelity simulations, however, are still used and recommended as cross-checks when possible. This approach will be implemented on the program to reduce the uncertainty currently carried by the flight dynamics tools using the CFD data for the full-scale Titan configurations.

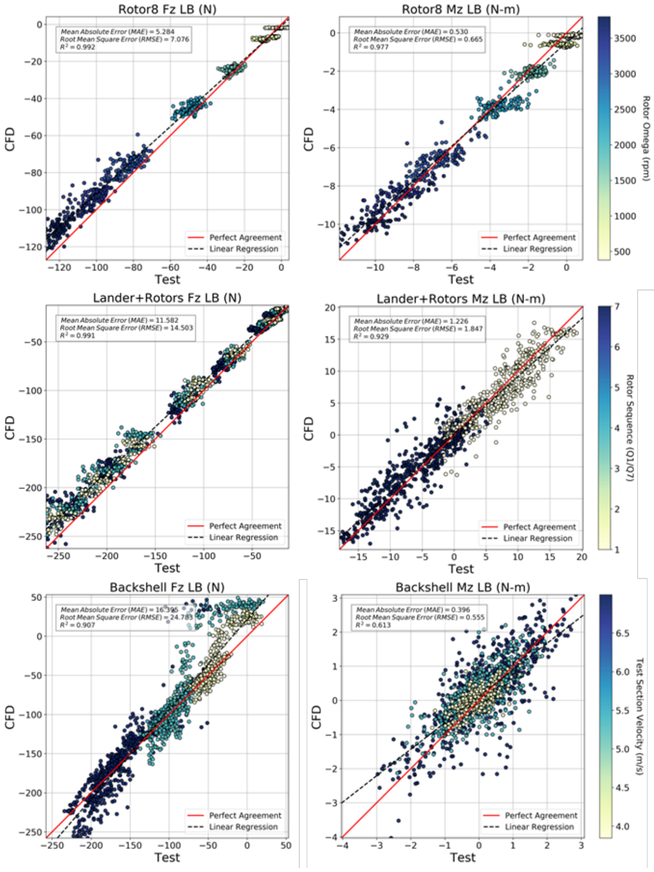

Figure 57. Test v. CFD parity plots for LRB F_z (left column) and M_z (right column), for R8 (top), LR (middle), and Backshell (bottom).

CONCLUSIONS

A 1/2 scale model of the Dragonfly PPF lander plus backshell configuration was tested in NFAC to determine its aerodynamic characteristics, emphasizing the ability of the rotors to generate a consistent yaw moment to counteract vehicle spin. Extensive Lander, Rotors and Backshell force, moment, and surface pressure data were obtained at over 13,000 conditions. In parallel, a Simcenter STAR-CCM+ CFD simulation of the as-built model in the test section was developed. The rotors were modeled using Blade Element Momentum Theory (BEMT) to provide a time-averaged actuator disk representation of each rotor that was coupled into the overall Navier Stokes flow solution. 1833 RANS-VDM cases were simulated for the LRB configuration.

The experiment successfully overcame several challenges:

1. Accurately measuring and maintaining low wind velocities in the test section using upstream towers with ultrasonic anemometers.

2. Measuring low magnitude aerodynamic loads relative to large gravitational and vibratory loads from structural modes and rotor harmonics. Acquiring data for 8 second blocks and filtering provided focus on the low frequency aerodynamics.

4. Synchronizing the multiple data streams from the NFAC and APL systems and parsing the 90 to 150 sec points into individual records for each rotor RPM.

5. Defining the experimental uncertainties driven by measurement precision plus low frequency load variation.

Specific experimental observations include:

1. The yaw moments, M_z, were categorized as <u>Favorable</u> (>80% of the hover M_z) at low V_∞ and/or low Pitch/Roll (<10-15°), <u>Reduced</u> at high V_∞ OR high Pitch/Roll (>20°), or <u>Adverse</u> (<15% or Swapped Sign) for High V_∞ AND high Pitch/Roll. The Backshell M_z magnitudes were generally small compared to the M_z from the Lander plus Rotors.

2. The individual rotors had consistent thrust and torque (~RPM^2) for almost all conditions. Thrust was reduced for some high V_∞, high Pitch/Roll conditions. Vortex ring state penetration is modest ($V_C/v_h > -0.8$) for combined lower V_∞ and higher rotor thrust, and substantial ($V_C/v_h < -2$) at combined high V_∞ and low thrust.

3. Lander lower surface pressures show relatively uniform positive pressures ($C_P > 0.5$) approaching stagnation at low rotor thrust, which transitions to suction ($C_P < -0.5$) for increased rotor thrust and induced velocity.

4. Lander left side suction pressures behind the rotors were consistent with the Lander reduced or adverse M_z, particularly for the Q1 sequences with the forward Rotor 5 active.

5. Backshell drag with the rotors off or at low thrust was consistent with that expected for an open cup, but it was reduced by aerodynamic interaction.at high thrust and |Pitch/Roll|<20°. At higher |Pitch/Roll|, the Backshell could maintain positive inner surface C_P and high drag. There were low frequency (<1Hz) F_z variations of substantial magnitude, mostly on the Backshell, at maximum V_∞ and maximum rotor thrust.

7. The Q1 and Q7 sequences with the two diagonal lower rotors active were most efficient generating M_z since they had canted thrust and shaft torque contributions aligned. Q5 with four diagonal rotors active and Q6 with four counterclockwise rotors active were less efficient than Q1 since either the shaft torque or the canted thrust contributions canceled and adverse Lander suction increased.

9. Although not a PPF rotor state, the A5 sequence with all eight rotors active has a very large effect reducing or reversing Backshell drag and increasing low frequency unsteady forces.

Specific CFD observations include:

1. Mid-fidelity modeling with RANS-VDM correlates well for the primary PPF objective: accurate LRB total M_z in support of the despin maneuver. The mean average error for Q1 and Q7 near the maximum M_z (+ or -17 Nm) was 2.1 Nm, which indicates a 12% error.

2. Higher fidelity CFD is required in conditions that stress the RANS-VDM underlying assumptions. IDDES-VDM significantly improves the correlation while still being less computationally expensive than simulations resolving the discrete rotor blade geometry.

ACKNOWLEDGMENTS

This work was conducted as part of the National Aeronautics and Space Administration Dragonfly Phase B contract N00024-13-D-6400 to the Johns Hopkins University Applied Physics Laboratory. Sikorsky's experimental data analysis and CFD simulation activities were funded through a subcontract from APL to Lockheed Martin Space.

Many people from each participating organization made essential contributions to the success of this effort. They include, but are not limited to, the following:

NASA: Bill Tomek, Jared Fell (Backshell Model Design), Steve Geissinger (Backshell Model Fabrication) (LaRC), Larry Young and Jason Cornelius (ARC).

APL: Matt Misiorowski, Stephanie Lepchenske, John Samsock, Chris Ward, Don Burton.

Sikorsky: Kate Gruber, Antonio Rivera, Katarina Trubelja, Maria Smerekanicz, William Welsh.

NFAC: Arturo Zamora, Jon Winegar, Daniel Brookbank, Johannes M. van Aken, Daniel Grieb, Emily Sayles, Chris Nykamp, Jose Cabrales, Meliton Abenojar, Pat Goulding II, Tyler Pearsall.

NAVAIR Applied Aerodynamics Branch: Mark Silva & Eric Hayden for loaning the anemometer arrays to the test effort.

Author Contacts:
Peter Lorber peter.f.lorber @lmco.com
Karl Edquist karl.t.edquist @nasa.gov
Brian McGrath brian.mcgrath @jhuapl.edu
Paul Gilles paul.gilles.ctr @us.af.mil

REFERENCES

1. **Lorenz, Ralph D.** *Dragonfly : Defining Environments for Rotorcraft Flight on Titan.* Virtual : Vertical Flight Society's 76th Annual Forum, Oct 9-11, 2020.

2. **Turtle, E.P., et al.** *Draonfly: Exploring Titan's Prebiotic Organic Chemistry and Habitability.* Woodlands, TX : Lunar and Planetary Science Conference XLVIII, 2017.

3. **Lorenz, R.** *Dragonfly : Entry and Descent one Titan Year after Huygens.* National Harbor, MD : AIAA SCITECH 2023 Forum, 2023. AIAA 2023-0599.

4. **Cornelius , J, et al.** *Dragonfly – Aerodynamics during Transition to Powered Flight.* Virtual : Vertical Flight Society's 77th Annual Forum, May 10-14, 2021.

5. **Marshall, M, et al.** *Performance of the Dragonfly Lander's Coaxial Rotor in Vortex Ring State.* Orlando, FL : AIAA SciTech Forum, 2024. 2024-0247.

6. **Zucker, C, et al.** *An assessment of Dragonfly-Backshell aerodynamics preparing for the initial flight on Titan.* s.l. : Acta Astronautica, 2024. doi.org/10.1016/j.actaastro.2024.07.046.

7. **Gruber, K., et al.** *The Evolution of Dragonfly's Design Using CFD at Titan.* Virginia Beach, VA : Vertical Flight Society 81st Annual Forum, 2025.

8. **Diaz, P.V., Edquist, C. and Yoon, S.** *High-Fidelity Computational Modeling of Dragonfly Lander during Preparation for Powered Flight.* Virginia Beach, VA : Vertical Flight Society 81st Annual Forum, 2025.

9. **Zell, Peter T.** *Performance and Test Section Flow Characteristics of the National Full-Scale Aerodynamics Complex 80- by 120-Foot Wind Tunnel.* s.l. : NASA, 1993. TM-103920.

10. **Berg, H and Tijdeman, H.** *Theoretical and Experimental Results for the Dynamic Response of Pressure Measuring Systems* . Amsterdam, Netherlands : National Aerospace Lab NLR-TR F-238, Jan., 1965.

11. **Cornelius, J and Schmitz, S.** *Coaxial Rotor CFD Validation and ML Surrogate Model Generation.* Santa Clara, CA : Vertical Flight Society Aeromeanics Specialists Conference, 2024.

12. **Leishman, J Gordon.** *Principles of Helicopter Aerodynamics.* New York : Cambridge University Press, 2006.

13. **Johnson, Wayne.** *Model for Vortex Ring State Influence on Rotorcraft Flight Dynamics.* s.l. : NASA, 2005. TP-2005-213477.

14. **Cornelius, J and Schmitz, S.** *Dragonfly Rotor Optimization using Machine Learning Applied to an OVERFLOW Generated Airfoil Database.* Montreal, Quebec : Vertical Flight Society 80th Annual Forum & Technology Display, 2024.

15. **Schmitz, S., et al.** *NASA Dragonfly Mission – Coaxial Rotor Test & CFD Prediction.* Virginia Beach, VA : Vertical Flight Society 81st Annual Forum, 2025.